Embedded-Oriented Open-Switch Fault Diagnosis and Localization for Dual Y-Connected PMSM Based on Deep Learning

Shihan Xu, Yuan Zhu, and Luca Zarri, *Senior Member, IEEE*

***Abstract*—The open-switch fault diagnosis speed of multiphase machines is generally no less than 1/4 of an electrical cycle, severely affecting the timeliness of fault-tolerant control intervention. To address this issue, this paper first proposes a cascaded triggering algorithm based on logical judgment, integrating optimized open-phase characteristic values with harmonic subspace current trajectories to enhance the stability of the logic-based method. The proposed data-driven method treats open-phase characteristic values and harmonic subspace currents as input features to reduce the computational burden of extracting open-circuit features in deep learning networks. In addition, to improve the computational speed of the neural network on embedded platforms, a multitarget classification network is designed based on a simplified gated unit, and a lightweight solving algorithm for the activation function is applied. The dataset used in the deep learning network is labeled with the assistance of a designed autoencoder while preserving the transition data between pre- and postfault states. The effectiveness, accuracy, and fault localization speed of the proposed algorithms are validated through the dataset and the experiment on the motor bench. The results demonstrate that the proposed data-driven method can accurately locate the open-switch fault within ten sampling periods.**

***Index Terms*—Data-driven method, dual *y*-connected permanent magnet synchronous motor (DY-PMSM), logic-based method, open-switch fault diagnosis.**

I. Introduction

DUAL *Y*-connected permanent magnet synchronous motor (DY-PMSM), due to its unique structure, offers inherent torque smoothness and fault tolerance. Given the high functional safety requirements for critical components in automotive systems, DY-PMSM is becoming the preferred solution for automotive steering and drive systems.

Received 12 June 2025; revised 11 September 2025 and 7 November 2025; accepted 5 December 2025. Date of publication 9 December 2025; date of current version 25 February 2026. This work was supported by the National Key Research and Development Program of China under Grant 2024YFB4007304. Recommended for publication by Associate Editor X. Zhang. *(Corresponding author: Yuan Zhu.)*

Shihan Xu and Yuan Zhu are with the Department of School of Automotive Studies, Tongji University, Shanghai 201804, China (e-mail: sh_xu@tongji.edu.cn; yuan.zhu@tongji.edu.cn).

Luca Zarri is with the Department of Electrical, Electronic and Information Engineering "G.Marconi", University of Bologna, 40136 Bologna, Italy (e-mail: luca.zarri2@unibo.it).

Color versions of one or more figures in this article are available at https://doi.org/10.1109/TPEL.2025.3641980.

Digital Object Identifier 10.1109/TPEL.2025.3641980

Common faults in the inverters and stator windings of PMSMs include short-circuit faults and open-circuit faults, which are generally caused by damage to the power components or driver circuits of the inverter [1]. Short-circuit faults are prone to overcurrent risks, and hardware protection circuits are often designed in inverters to achieve electrical isolation [2], thereby converting short-circuit faults into open-circuit faults. Open-circuit faults can cause torque pulsations in multiphase motors, affecting the system's operational performance. Although multiphase machines inherently offer fault-tolerant operation, it is essential to rapidly identify the open-switch fault to provide reliable prior information for fault-tolerant control [3]. Some studies have proposed unified controllers that eliminate the need for fault diagnosis and mode switching between normal and faulty states [4], [5], but the postfault performance of the system remains limited. Given the high functional safety requirements of automotive components, the ability to accurately locate the fault enables the controller to adjust control strategies while also guiding component maintenance and replacement.

In open-circuit fault diagnosis, many effective methods have been proposed. Among fault diagnosis algorithms based on the three-phase topology, the method that directly calculates the root-mean-square (RMS) value of the phase current to detect open-circuit faults is simple, intuitive, and easy to implement. However, it is prone to misjudgment under low-current conditions and exhibits a relatively slow diagnostic speed [6]. Salman et al. [7] achieved fast open-circuit fault localization by calculating the rms of each phase power. However, this method requires accurate threshold calibration based on the motor torque and speed. In addition, the deviation between the actual and predicted currents in the synchronous rotating reference frame (SRRF) can serve as an indicator for open-circuit fault diagnosis [8], [9]. Similarly, Hang et al. [10] set open-circuit thresholds for the dc and second-harmonic currents included in the cost function of the designed predictive control. This method uses the initial phase angle of the phase current to achieve open-circuit fault localization. A more straightforward and reliable approach involves directly measuring the voltage on both sides of the switching device and comparing it with the command of the upper level controller [11], [12]. However, this method requires modifications to the hardware circuitry, leading to increased hardware costs.

In designing fault diagnosis indicators based on the structural characteristics of multiphase machines, the vector space decomposition (VSD) transformation introduces a harmonic current subspace, allowing the application of reference-to-actual current comparison methods to harmonic currents, thereby improving diagnostic stability [13]. In addition, the harmonic subspace current trajectory angle [14], [15] and its relationship with the fundamental current [16] effectively indicate the location of open-circuit faults. Building on this principle, Wu et al. [17], [18] performed multiharmonic subspace currents analysis for six-phase motors and achieve accurate diagnosis and localization in variable-phase-pole machines by combining multiple harmonic subspace current trajectories. Li et al. [19] determined the machine's health status by observing the elliptical current trajectory in the stator reference frame after an open-circuit fault in a five-phase machine, and localize the fault using the third-harmonic current in the SRRF. However, this method requires running through five sectors for a complete detection cycle, leading to a relatively slow diagnosis speed. In contrast to harmonic subspace-based methods, Chen et al. [20] analyzed the abnormal magnetic field pendulous oscillation (MFPO) phenomenon caused by open-phase faults to diagnose both single-phase and two-phase combined open-circuit faults in five-phase machines. However, this method requires calculating the maximum MFPO angle within one electrical cycle, resulting in relatively low diagnosis timeliness. Gardouh et al. [21] leveraged the normalized dc components of stator line currents and the normalized negatively oriented dc components of motor line currents in the SRRF to locate the open-circuit fault. However, this method requires a detection delay exceeding one electrical cycle.

The above-mentioned methods can generally be categorized into model-based methods [8], [9], [10], [13] and signal-based methods [6], [14], [15], [16], [18], [19], [20]. Among them, methods using the phase current rms value or reference current comparison are prone to misjudgment when the PMSM operates under low torque, as in most cases of open-switch faults, the freewheeling diode can still conducts [22]. On the other hand, signal-based methods that design characteristic values or diagnose open-circuit faults based on harmonic current variations typically rely on threshold-based judgments, which results in slower diagnosis. In recent years, numerous studies introduce data-driven methods into open-circuit fault diagnosis to enhance diagnostic accuracy. However, certain approaches employing fast Fourier transform [23], [24] and multilayer convolutional neural networks [25], [26], [27] as feature extraction techniques incur significant computational overhead and makeing it difficult to achieve rapid fault identification. To reduce the runtime of data-driven algorithms, Rokocakau et al. [28] designed three shallow neural networks for fault detection and localization. The proposed algorithm achieves an average computation time of 39 μs on FPGA devices, providing high accuracy with minimal computational burden. Jin et al. [29], [30] considered the limited training dataset, design online data-driven semisupervised fault diagnosis methods for three-phase PMSM, they use phase current as the main input feature, and for six-phase PMSM, they use harmonic subspace current as the main input feature. According to experimental results, the proposed methods quickly reflect fault states but require more than half an electrical cycle to locate open-circuit faults. Liu et al. [31] used deep sparse filtering to abstract sample features, suppressing irrelevant variable data and amplifying relevant data. The proposed method achieves an accuracy of 99.56% in open-circuit fault diagnosis for six-phase machines.

TABLE I
COMPARISON OF OPEN-CIRCUIT FAULT DIAGNOSTIC METHODS

Method	Number of phases	Detection parameter	Detection delay
RMS (phase power) [7]	3	phase current and voltage	$< \frac{1}{4}$
current deviation [8]	3	dq-axis current	$\frac{1}{4} \sim \frac{1}{2}$
current deviation (cost function) [10]	3	dq-axis current	$\frac{1}{2} \sim 1$
current trajectory [14]	6	harmonic current	≈ 1
current trajectory [15], [19]	5	harmonic current	$\approx \frac{1}{4}$, ≈ 1
current trajectory [17], [18]	variable	harmonic current	$< \frac{1}{4}$
construct feature value [16]	6	subspace current	$\frac{1}{4} \sim 1$
construct feature value (MFPO) [20]	5	stator current	≈ 1
construct feature value [21]	3	phase current and speed	> 1
data-driven [23], [24]	3	phase current	$\frac{1}{4} \sim 1$
data-driven [29]	6	harmonic current	$\frac{1}{2} \sim 1$
data-driven [30]	6	torque and position	$\frac{3}{4} \sim 1$
data-driven [31]	6	phase current	$\frac{1}{2} \sim 1$

Table I summarizes the methods cited in this article, including the number of motor phases, detection parameters, and the number of electrical cycles for fault detection delay. Based on Table I and the above-mentioned analysis, data-driven methods demonstrate high performance in open-circuit fault diagnosis. However, many studies rely on DSP and FPGA platforms, which make them difficult to implement in automotive chassis and drive systems. The study in this article aims to achieve fast and accurate open-switch fault diagnosis on automotive embedded platforms, mitigating the impact of torque ripple caused by open-switch faults on components with high functional safety requirements.

The main contributions and advantages investigated in this article are as follows.

1) The impact of sensor gain errors on fault diagnosis is considered and mitigated.

2) By combining the characteristic value and harmonic current trajectory methods, the stability of open-switch fault diagnosis is enhanced. More importantly, a lightweight neural network is developed that delivers high accuracy and rapid detection.

3) The proposed lightweight data-driven algorithm can be deployed on the Infineon TC399xp embedded platform a computation time of less than 50 μ s.

The rest of this article is organized as follows. Section II analyzes and addresses the impact of phase current sensor gain errors on open-phase characteristic values. A stable and fast cascaded triggering logic-based diagnosis method is proposed

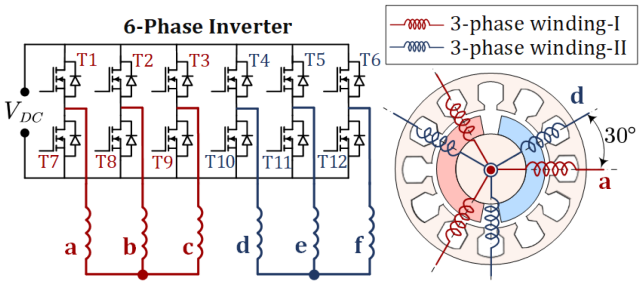

Fig. 1. DY-PMSM with 30° phase-shift.

by combining the harmonic subspace current trajectory method. Section III first designs an autoencoder to directly detect anomalies in open-switch test data to solve the cumbersome dataset labeling problem. Then, a lightweight neural network classifier and a fast activation function calculation method are designed for embedded system applications. Section IV compares the proposed logic-based method and data-driven method through experiments on a DY-PMSM test bench. Finally, Section V concludes this article.

II. Logic-Based Open-Switch Location Method

A. Open-Phase Fault Characteristic Value

In the phase-shifted 30° DY-PMSM shown in Fig. 1, the VSD transformation in (1) is typically used to decompose the six-phase currents into three orthogonal vector subspaces. Here, the superscript "s" represents the stator stationary reference frame

$$\boldsymbol{i}_h^s = \frac{1}{3}\sum_{k=1}^{3}\left(\boldsymbol{i}_{\mathrm{I}}(k) + \boldsymbol{i}_{\mathrm{II}}(k)e^{j\frac{\pi}{6}}\right)e^{j\frac{2\pi}{3}h(k-1)} \quad h = 1, 3, 5 \tag{1}$$

where $\boldsymbol{i}_{\mathrm{I}} = [i_a, i_b, i_c]^T$ and $\boldsymbol{i}_{\mathrm{II}} = [i_d, i_e, i_f]^T$.

The phase currents can be decomposed into the stator current subspace $\boldsymbol{i}_1^s = [i_\alpha^s, i_\beta^s]^T$, the zero current subspace $\boldsymbol{i}_3^s = [i_{o1}^s, i_{o2}^s]^T$, and the harmonic current subspace $\boldsymbol{i}_5^s = [i_x^s, i_y^s]^T$ by (1). Based on the winding distribution and connection form of the phase-shifted 30° DY-PMSM, it is known that $\boldsymbol{i}_3^s = 0$ under normal operating conditions. For simplification, (1) can be rewritten as follows:

$$\begin{bmatrix} \boldsymbol{i}_1^s \\ \boldsymbol{i}_5^s \\ \boldsymbol{i}_3^s \end{bmatrix} = T_6^s \begin{bmatrix} \boldsymbol{i}_{\mathrm{I}} \\ \boldsymbol{i}_{\mathrm{II}} \end{bmatrix} \tag{2}$$

where

$$T_6^s = \frac{1}{3}\begin{bmatrix} 1 & -\frac{1}{2} & -\frac{1}{2} & \frac{\sqrt{3}}{2} & -\frac{\sqrt{3}}{2} & 0 \\ 0 & \frac{\sqrt{3}}{2} & -\frac{\sqrt{3}}{2} & \frac{1}{2} & \frac{1}{2} & -1 \\ 1 & -\frac{1}{2} & -\frac{1}{2} & -\frac{\sqrt{3}}{2} & \frac{\sqrt{3}}{2} & 0 \\ 0 & -\frac{\sqrt{3}}{2} & \frac{\sqrt{3}}{2} & \frac{1}{2} & \frac{1}{2} & -1 \\ 1 & 1 & 1 & 0 & 0 & 0 \\ 0 & 0 & 0 & 1 & 1 & 1 \end{bmatrix}. \tag{3}$$

By combining (2) and (3), the equation for calculating phase currents from $\boldsymbol{i}_1^s$, $\boldsymbol{i}_5^s$, and $\boldsymbol{i}_3^s$ can be obtained as follows:

$$\begin{bmatrix} i_a \\ i_b \\ i_c \\ i_d \\ i_e \\ i_f \end{bmatrix} = \begin{bmatrix} i_\alpha^s + i_x^s + i_{o1}^s \\ -\frac{1}{2}i_\alpha^s + \frac{\sqrt{3}}{2}i_\beta^s - \frac{1}{2}i_x^s - \frac{\sqrt{3}}{2}i_y^s + i_{o1}^s \\ -\frac{1}{2}i_\alpha^s - \frac{\sqrt{3}}{2}i_\beta^s - \frac{1}{2}i_x^s + \frac{\sqrt{3}}{2}i_y^s + i_{o1}^s \\ \frac{\sqrt{3}}{2}i_\alpha^s + \frac{1}{2}i_\beta^s - \frac{\sqrt{3}}{2}i_x^s + \frac{1}{2}i_y^s + i_{o2}^s \\ -\frac{\sqrt{3}}{2}i_\alpha^s + \frac{1}{2}i_\beta^s + \frac{\sqrt{3}}{2}i_x^s + \frac{1}{2}i_y^s + i_{o2}^s \\ -i_\beta^s - i_y^s + i_{o2}^s \end{bmatrix}. \tag{4}$$

The fifth-order harmonic currents i_x^s and i_y^s are typically regulated to zero using the proportional-resonant controller to reduce torque ripple and Joule losses [32]. Under open-switch fault conditions, the introduced fundamental current components within the harmonic subspace will not be suppressed by the proportional-resonant controller, causing a sudden increase in current magnitude. Therefore, based on (4), the current components of the $\boldsymbol{i}_5^s$ and $\boldsymbol{i}_1^s$ in each phase current can be separated, and the characteristic value for open-phase fault identification is designed as the ratio of the $\boldsymbol{i}_5^s$ to $\boldsymbol{i}_1^s$ currents, as shown in

$$C_a = -\frac{i_x^s}{i_\alpha^s}, C_b = \frac{i_x^s + \sqrt{3}i_y^s}{-i_\alpha^s + \sqrt{3}i_\beta^s}, C_c = \frac{i_x^s - \sqrt{3}i_y^s}{-i_\alpha^s - \sqrt{3}i_\beta^s},$$
$$C_d = \frac{\sqrt{3}i_x^s - i_y^s}{\sqrt{3}i_\alpha^s + i_\beta^s}, C_e = \frac{\sqrt{3}i_x^s + i_y^s}{\sqrt{3}i_\alpha^s - i_\beta^s}, C_f = -\frac{i_y^s}{i_\beta^s}. \tag{5}$$

Taking phase-c and phase-f as examples, when an open-circuit fault occurs in phase-c, substituting (2) into (5) and applying Kirchhoff's current law (KCL), (6) can be obtained as follows:

$$C_c = \frac{i_x^s - \sqrt{3}i_y^s}{-i_\alpha^s - \sqrt{3}i_\beta^s} = \frac{(i_a + i_b) - \sqrt{3}i_d + \sqrt{3}i_f}{\underbrace{-(i_a + i_b)}_{=0} - \sqrt{3}i_d + \sqrt{3}i_f} = 1. \tag{6}$$

Similarly, when an open-circuit fault occurs in phase-f, (7) can be obtained

$$C_f = \frac{-i_y^s}{i_\beta^s} = \frac{\sqrt{3}(i_b - i_c) - (i_d + i_e)}{\sqrt{3}(i_b - i_c) + \underbrace{(i_d + i_e)}_{=0}} = 1. \tag{7}$$

From (5) to (7), the open-phase characteristic values in (5) are nearly zero under normal operating conditions and reach 1 when the phase has an open-circuit fault. This provides an effective indication of the open-circuit fault status for each phase.

B. Impact of Phase Current Sensor Gain Error and Countermeasures

Nonideal operating conditions of the current measurement circuit, such as the nonlinearity of current sensors, inaccuracy of resistances in the analog filters, measurement resistors, and the quantization errors of the A/D converters, cause current measurement errors [33]. Multiphase machines operate under harsh conditions where varying component losses across phases make current sensors more prone to errors. Among these, gain error is particularly challenging to identify through online diagnosis. When performing an open-circuit fault diagnosis, it is essential to consider the potential interference caused by current sensor gain errors.

Let the measured six-phase currents be denoted as $[\boldsymbol{i}_{\mathrm{I},m}, \boldsymbol{i}_{\mathrm{II},m}]^T$. Under the VSD transformation, the relationship between the measured subspace currents and the actual phase currents is given by

$$T_6^{s-1}\begin{bmatrix} \boldsymbol{i}^s_{1,m} \\ \boldsymbol{i}^s_{5,m} \\ \boldsymbol{i}^s_{3,m} \end{bmatrix} = \begin{bmatrix} \boldsymbol{i}_{\mathrm{I},m} \\ \boldsymbol{i}_{\mathrm{II},m} \end{bmatrix} = \begin{bmatrix} \boldsymbol{K}_1 & 0 \\ 0 & \boldsymbol{K}_2 \end{bmatrix} \begin{bmatrix} \boldsymbol{i}_{\mathrm{I}} \\ \boldsymbol{i}_{\mathrm{II}} \end{bmatrix} \tag{8}$$

where

$$\begin{cases} \boldsymbol{K}_1 &= \begin{bmatrix} k_a & k_b & k_c \end{bmatrix} \boldsymbol{I}_3 \\ \boldsymbol{K}_2 &= \begin{bmatrix} k_d & k_e & k_f \end{bmatrix} \boldsymbol{I}_3. \end{cases} \tag{9}$$

In (9), $\boldsymbol{K}_1$ and $\boldsymbol{K}_2$ represent the gain error matrices of the winding-I and winding-II phase currents, respectively.

Substituting (9) into (8), combined with KCL, the measured value of the zero current subspace can be obtained as follows:

From (10) shown at the bottom of this page, it can be seen that when $k_a = k_b = k_c = 1$ and $k_d = k_e = k_f = 1$, $\boldsymbol{i}^s_{3,m} = 0$ can be calculated. However, when current sensor gain errors exist, $\boldsymbol{i}^s_{3,m} \neq 0$ is obtained. Therefore, when constructing the open-phase characteristic value, the zero current subspace must be considered. Based on the analysis of sensor gain error propagation, the open-phase characteristic value is optimized to (11) using (4)

$$\begin{aligned} C_A &= -\frac{i^s_x + i^s_{o1}}{i^s_\alpha}, & C_D &= \frac{\sqrt{3}i^s_x - i^s_y - 2i^s_{o2}}{\sqrt{3}i^s_\alpha + i^s_\beta} \\ C_B &= \frac{i^s_x + \sqrt{3}i^s_y - 2i^s_{o1}}{-i^s_\alpha + \sqrt{3}i^s_\beta}, & C_E &= \frac{\sqrt{3}i^s_x + i^s_y + 2i^s_{o2}}{\sqrt{3}i^s_\alpha - i^s_\beta} \\ C_C &= \frac{i^s_x - \sqrt{3}i^s_y - 2i^s_{o1}}{-i^s_\alpha - \sqrt{3}i^s_\beta}, & C_F &= -\frac{i^s_y - i^s_{o2}}{i^s_\beta}. \end{aligned} \tag{11}$$

Taking the case where winding-I has gain errors and phase-a undergoes an open-circuit fault as an example in the simulation, Fig. 2 compares the feature value of phase-a under different gain error settings.

From Fig. 2, it can be observed that when there is no current sensor gain error, the results from (5) and (11) are consistent. However, when a gain error occurs in winding-I, C_a exhibits distortion with changes in the electrical angle during the phase-a open-circuit fault, especially as shown in Fig. 2(c), whereas C_A remains stable in representing the open-circuit fault status. Moreover, under different error sets shown in Fig. 2, C_A is almost identical under open-circuit fault conditions, indicating the necessity of considering the interference from current sensor gain error in the open-phase feature value.

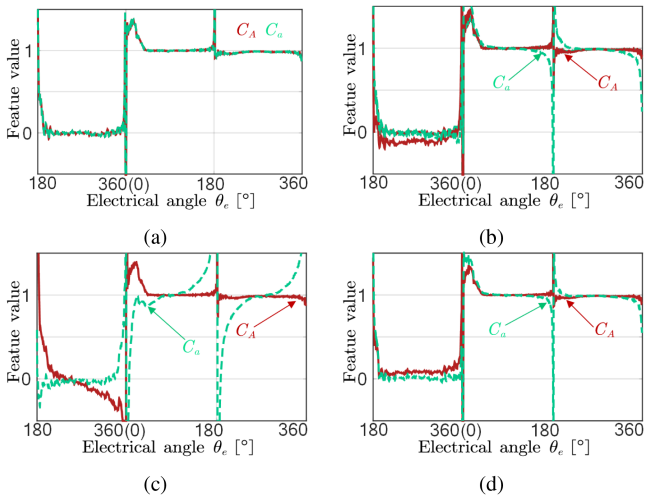

Fig. 2. Open-phase feature value of phase-a. (a) Without the current sensor gain error. (b) Winding-I with gain errors set as $k_a = 1.2$, $k_b = 0.9$, and $k_c = 1.0$. (c) Winding-I with gain errors set as $k_a = 1.1$, $k_b = 1.2$, and $k_c = 0.78$. (d) Winding-I with gain errors set as $k_a = 0.88$, $k_b = 1.05$, and $k_c = 1.11$.

C. Current Trajectory of Harmonic Subspace Under Open-Switch Fault

Compared to traditional fault diagnosis methods based on the rms of phase currents, the methods based on open-phase characteristic values described in Section II-B identify open-circuit faults by utilizing the appearance of fundamental-frequency components with relatively large magnitudes in the harmonic current subspace during fault conditions. Therefore, in theory, the faulty bridge arm can also be located based on the variations in the harmonic current trajectories.

Considering the individual open-circuit faults of the twelve switches in a six-phase system, 12 fault states can be identified and localized using the current trajectory method. Based on (2), (3), and the six-phase winding distribution form shown in Fig. 1, the harmonic current trajectory during an open-circuit fault can be decomposed into three coordinate systems based on the i^s_x-i^s_y subspace. As shown in Fig. 3(a), the rotated frame is spaced at 120° and 240° relative to the i^s_x-i^s_y subspace [14].

In practice, due to factors such as current fluctuations, inverter errors, and the quality of current loop control, the i^s_x-i^s_y subspace current trajectories for each switch open-circuit will deviate from the theoretical current trajectory shown in Fig. 3(a). In

$$\begin{aligned} i^s_{o1,m} &= \frac{\left(\frac{1}{k_a} - \frac{1}{2k_b} - \frac{1}{2k_c}\right)\left(i^s_{\alpha,m} + i^s_{x,m}\right) + \left(\frac{\sqrt{3}}{2k_b} - \frac{\sqrt{3}}{2k_c}\right)\left(i^s_{\beta,m} - i^s_{y,m}\right)}{-\left(\frac{1}{k_a} + \frac{1}{k_b} + \frac{1}{k_c}\right)} \\ i^s_{o2,m} &= \frac{\left(\frac{\sqrt{3}}{2k_d} - \frac{\sqrt{3}}{2k_e}\right)\left(i^s_{\alpha,m} - i^s_{x,m}\right) + \left(\frac{1}{2k_d} + \frac{1}{2k_e} - \frac{1}{k_f}\right)\left(i^s_{\beta,m} + i^s_{y,m}\right)}{-\left(\frac{1}{k_d} + \frac{1}{k_e} + \frac{1}{k_f}\right)}. \end{aligned} \tag{10}$$

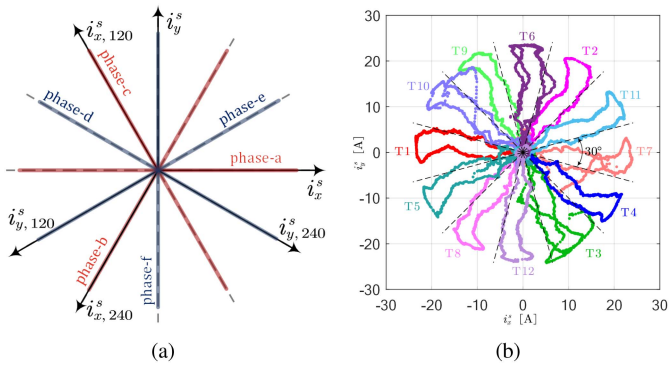

(a) (b)

Fig. 3. Current trajectories in the i_x^s-i_y^s subspace for open-circuit faults. (a) Theoretical current trajectories. (b) Real current trajectories obtained from open-switch testing on DY-PMSM.

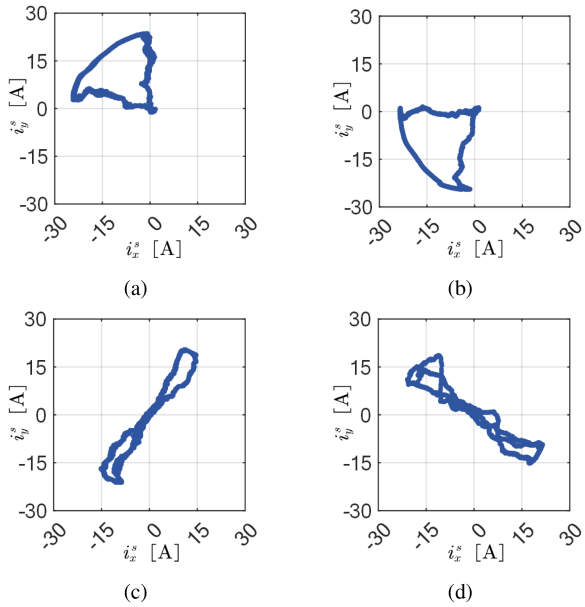

(a) (b) (c) (d)

Fig. 4. i_x^s-i_y^s current trajectory when two-switches are open-circuited. (a) T1–T6 with open-circuit fault. (b) T1–T12 with open-circuit fault. (c) T2–T8 with open-circuit fault. (d) T4–T10 with open-circuit fault.

some cases, these trajectories may even exceed the range of 30°. Fig. 3(b) shows the i_x^s-i_y^s subspace current trajectories measured when the phase current magnitude is 24.5A and when each of the twelve switches is open-circuited individually. These trajectories do not follow the ideal path in Fig. 3(a). The current scatter plots for T3, T7, and T10 open-circuit faults in Fig. 3(b) show that a sudden open-circuit fault occurring under large phase current causes the i_x^s-i_y^s subspace current trajectory to exhibit significant oscillations.

Due to the numerous possible cases of two-switch open-circuit faults, only four cases are presented in Fig. 4, including the i_x^s–i_y^s subspace current trajectories for the open-circuit faults of T1–T6, T1–T12, T2–T8, and T4–T10.

As evidenced by Fig. 4, when both open-circuit switches belong to the same phase, the current trajectory is almost a straight line. However, when switches from different phases

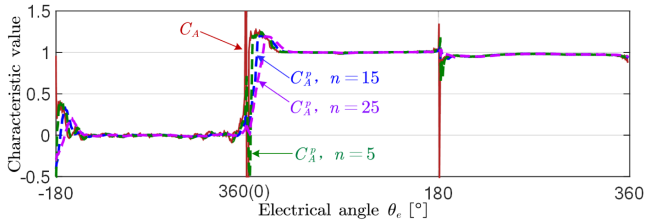

Fig. 5. Comparison of feature values under different parameter n.

experience open-circuit faults, the current trajectory forms a sector shape, with the starting and ending angles closely related to the single-switch open-circuit trajectories in Fig. 3. In [34], the current trajectories for two-switch open-circuit faults are categorized into six types. In essence, these cases are merely combinations of the single-switch fault trajectories shown in Fig. 3. Regardless of how the fault cases are classified, the fundamental principle remains the same as identifying the fault location by analyzing the current trajectory and mapping it to the corresponding faulty switches.

D. Cascaded Triggering Logic-Based Open-Switch Location Method

From Fig. 2, significant oscillations occur when the denominator of the designed characteristic value approaches zero, rendering fault diagnosis unreliable. To stabilize the feature value and improve reliability, (12) introduces a sliding window mean filtering strategy with extremum elimination

$$C_*^p = \frac{\sum_{i=1}^{n} \boldsymbol{C}_*(i) - \max(\boldsymbol{C}_*) - \min(\boldsymbol{C}_*)}{n-2} \tag{12}$$

where $n = \text{length}(\boldsymbol{C}_*)$, $* = A, B, \ldots F$, and $\boldsymbol{C}_*$ is an n-dimensional vector formed by C_* through $n-1$ time delays.

The comparison of feature values before and after the signal stabilization strategy is shown in Fig. 5. As shown in Fig. 5, increasing n smooths C_A^p and suppresses oscillations near the current zero-crossing. However, an excessively large n reduces the variation rate of C_A^p, which will introduce a delay in fault detection. Therefore, selecting an appropriate value of n according to the specific application can effectively improve fault detection stability while minimizing detection delay.

In Fig. 3, the i_x^s–i_y^s current trajectories with open-switch faults do not always stay within the ideal sector. Therefore, using the current trajectory to locate the fault has low accuracy and reliability. In the logic-based method, this article proposes the cascaded triggering structure shown in Fig. 6. By detecting open-phase faults, the fault location coordinate is expanded, and the i_x^s–i_y^s currents are converted to a polar coordinate to reduce the complexity of the logic-based method. In Fig. 6, $i_{5,\theta}^s$ and $i_{5,r}^s$ represent the polar angle and polar radius of the i_x^s–i_y^s current trajectory, respectively.

Fig. 7 takes the T1 open-circuit as an example. After the controller detects the open-phase fault, the fault is located between the T1 and T7 switches. At this point, the 30° polar angle range is expanded to 150°, and the open-switch is located by the current polar angle.

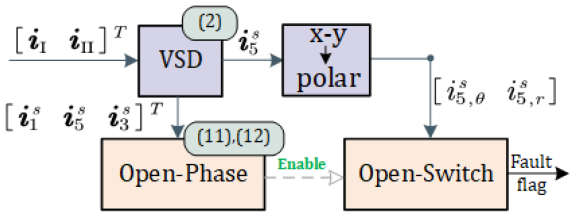

Fig. 6. Diagram of the logic-based cascaded triggering method for open-switch fault location.

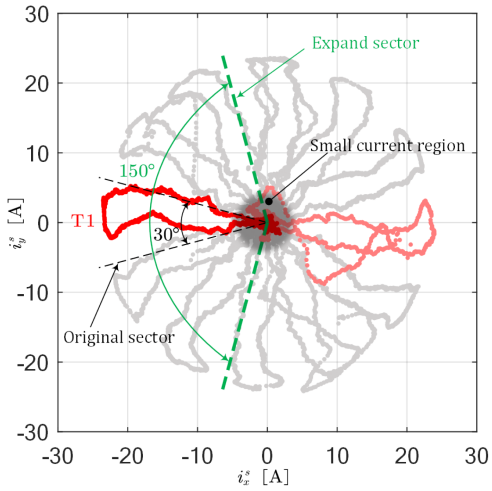

Fig. 7. Comparison of T1 open-circuit detection sector before and after expansion.

From Fig. 7, it can be concluded that the current trajectories outside the small current region and within the expanded sector can be identified as T1 open-circuit faults, effectively improving the stability and accuracy of open-switch localization. Although the cascaded diagnostic structure significantly expands the sector identification range for open-switch trajectories and mitigates the impact of polar angle fluctuations, the current magnitude of open-switch faults under low-current conditions remains difficult to distinguish from that of healthy state harmonic currents using threshold-based methods.

III. Proposed Data-Driven Method

The localization of an open-switch fault is essentially a multiple-classification problem of the operating state of a discrete system with multiple reference value inputs. By analyzing the variation of input variables, the correlation with the operating state is abstracted, thus solving the fault localization problem. However, the neural network training process relies on accurate data labeling. Therefore, the deep neural network-based open-switch localization method proposed in this article first employs an autoencoder-based offline anomaly detection to assist in dataset labeling. For online fault localization, a simple, lightweight network is designed based on the memoryless gated recurrent unit (GRU) and multilayer perceptron (MLP) to improve online operational efficiency.

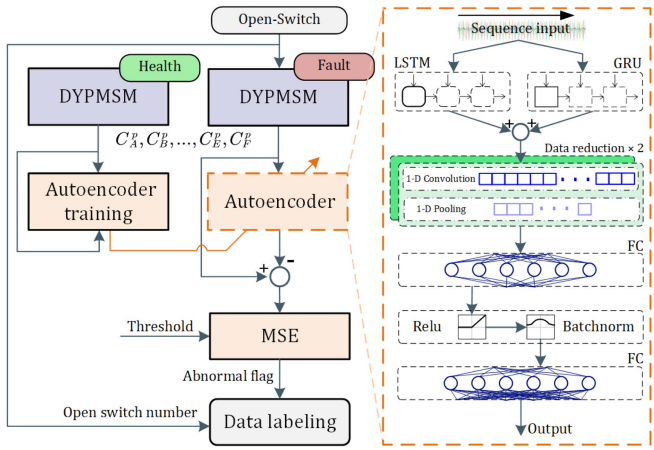

Fig. 8. Proposed DY-PMSM open-switch fault data labeling method and the autoencoder structure, where LSTM denotes the long short-term memory layer and FC denotes the fully connected layer.

A. Offline Dataset Labeling Method Based on Proposed Autoencoder

An open-switch fault only affects the operating state when the faulty switch is conducting. Directly using the open-circuit command issued during testing as a fault label will contaminate the dataset. Comparing the switch output voltage with its ideal value requires additional voltage sensors and must account for inverter dead-time effects. Moreover, using other diagnostic methods, such as the method proposed in Section II-D as a dataset labeling approach, may introduce coupling between the trained network's performance and the logic-based diagnostic method.

To address the challenge of fault dataset labeling, this article proposes the data labeling process shown in Fig. 8 along with the designed autoencoder structure. The data dimensions of this network are provided in Appendix A1. The training data for the autoencoder is collected during the normal operation of the DY-PMSM, which is easy to obtain.

During the autoencoder training, the open-phase fault characteristic values serve as both the input and output. In the prediction process, due to the Autoencoder's feature extraction capability, the mean square error (MSE) of fault data input increases sharply compared to normal data input, making it highly sensitive to anomalies. However, the autoencoder can only detect anomalies in the input data. To locate the anomalous switch, it must be combined with the corresponding open-switch number.

Fig. 9 illustrates the gated mechanisms of LSTM and GRU layers. The gated mechanism preserves highly correlated features while discarding less relevant ones, effectively enhancing the information contained in the input sequence. As shown in their structures, LSTM selectively outputs part of the state while using the cell state as an information carrier across LSTM units. In contrast, GRU outputs the entire state and passes it between units, offering advantages such as fewer parameters and faster convergence. In Fig. 8, the outputs of LSTM and GRU are combined to leverage the fast convergence capability of GRU and its backpropagation mechanism, accelerating the

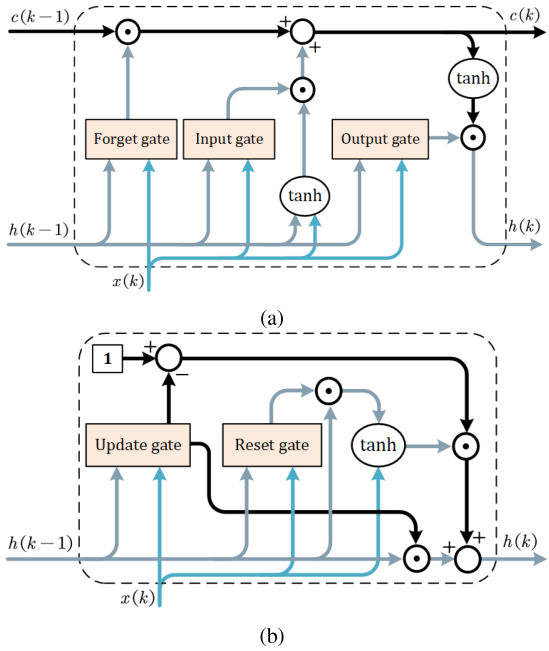

Fig. 9. Basic unit structure. (a) LSTM unit. (b) GRU unit.

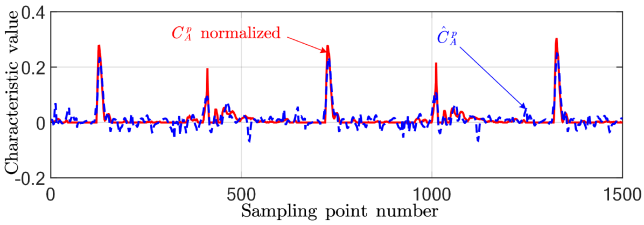

Fig. 10. Input and predicted output of autoencoder, using healthy status data of phase-a as an example.

parameter convergence of the autoencoder. The feature information extracted by LSTM and GRU is further refined in the convolutional neural network, mapped to a high-dimensional space, and ultimately re-extracted into six predicted values to fit the input features.

The valid range of the input open-phase feature value "C_*^p" is [0,1]. However, minor fluctuations may occur due to discrepancies between the actual and idealized models. Therefore, the normalization range of "C_*^p" is set to [0,1.2]. Fig. 10 illustrates the fitting performance of the designed autoencoder output $\hat{C}_A^p$ to the normalized open-phase characteristic value under the healthy condition of phase-a. It can be observed that despite the high nonlinearity of C_A^p, the autoencoder effectively tracks the input trend with minimal overall error.

The healthy datasets used to train the autoencoder were collected under healthy operating conditions at four current operating points for 100 and 200 rpm, respectively. At each operating point, 0.5 s of steady-state data was extracted. The four operating points are: 1) $i_d^* = -0.5$ A, $i_q^* = 7$ A; 2) $i_d^* = -1$ A, $i_q^* = 10$ A; 3) $i_d^* = -1.5$ A, $i_q^* = 13$ A; and 4) $i_d^* = -2$ A, $i_q^* = 16$ A, where i_d^* and i_q^* denote the current commands in the SRRF.

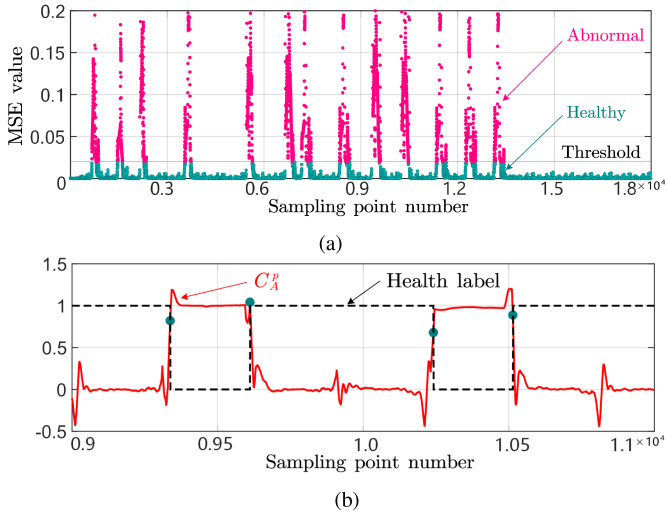

Fig. 11. (a) MSE between the autoencoder input and output with health and open-switch data input. (b) Comparison between C_A^p and health label predicted by autoencoder when phase-a has an open-switch fault, the sampling point number is in the range of [0.9,1.1] $\times 10^4$.

During the offline prediction in the open-circuit dataset, the MSE between the autoencoder's output and input features is calculated using (14). The MSE obtained when feeding the phase-a open-circuit fault data into the autoencoder is shown in Fig. 11(a). The MSE is not only used to determine the threshold for anomaly data but also serves as the evaluation metric during the training of the autoencoder. Since "C_*^p"$\in [0, 1.2]$, a reconstruction error of $|C_*^p - \hat{C}_*^p| < 0.1$ theoretically indicates satisfactory fitting performance. From (14), the training criterion of the autoencoder is obtained as MSE < 0.01, while the threshold for anomaly data is set empirically as twice this value. When the anomaly value exceeds the threshold, the health label is set to 0. Fig. 11(b) illustrates the health label identified by the autoencoder when an open-circuit occurs in phase-a

$$\text{MSE} = \frac{1}{6}\sum_{*=A}^{F}\left(C_*^p - \hat{C}_*^p\right)^2. \tag{13}$$

From Fig. 11(a), it can be observed that the autoencoder is highly sensitive to anomalous data. When abnormal data are input, the autoencoder produces an output significantly different from the input feature. Therefore, calculating the MSE and simply setting a threshold allows for the classification of anomalies and healthy data. As shown in Fig. 11(b), the health label is obtained not by directly applying a hard threshold to C_A^p but rather by computing the MSE between the autoencoder's input and predicted values. Setting a threshold on the MSE reduces the impact of C_A^p fluctuations on health state transitions. However, the autoencoder can only distinguish the healthy state of the DY-PMSM and cannot directly label the fault location. Therefore, dataset labeling must incorporate the open-switch fault command during data acquisition. This enables rapid labeling of the training dataset, providing an accurate and effective dataset for the open-switch fault localization algorithm.

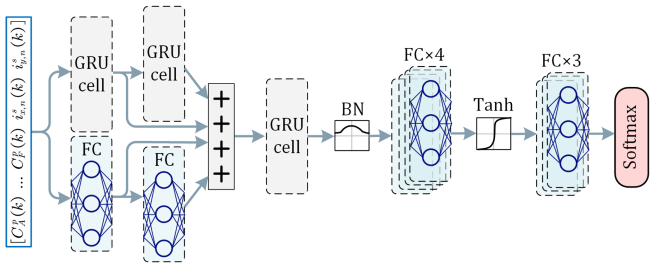

Fig. 12. Proposed network structure for classification.

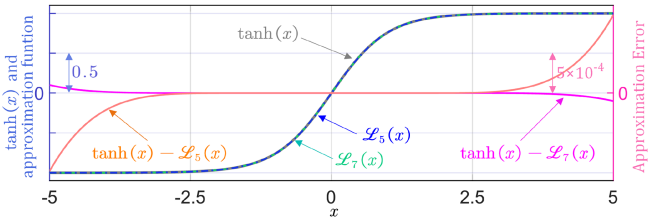

Fig. 13. Error of approximate function.

TABLE II
PMSM TEST BENCH PARAMETERS

Parameters	Quantity	Parameters	Quantity
Rated power	400W	Number of pole pairs	5
Dc link voltage	12V	Number of neutral-point	2
Rated speed	1000rpm	PWM frequency	20 kHz
Phase shift	30°	Sampling period	50 μs

B. Proposed Lightweight Open-Switch Fault Location Network

Deep neural networks typically have multilayer structures, complex computational processes, and a large number of multiplications and exponential operations. These complexities make it challenging for embedded platforms in the automotive chassis domain to provide sufficient computational resources. To reduce the computational burden while ensuring accurate open-circuit fault localization, this article designs the network structure shown in Fig. 12, and the data dimensions of this network are provided in Appendix A2.

Unlike the autoencoder, which uses sequence signals as input, the classification network shown in Fig. 12 only takes the current sampling point data as input features. This is because using sequence signal inputs in an embedded platform would require processing historical information, significantly increasing computational complexity.

In the input features, $i^s_{5,\theta}$ exhibits strong nonlinearity in polar coordinates, and undergoes rapid variations, which makes it difficult for the neural network to effectively extract useful information. In addition, since open-switch faults introduce fundamental components into $\boldsymbol{i}^s_5$, normalization of i^s_x and i^s_y is performed using (14). Taking $i^s_{x,n}$ and $i^s_{y,n}$ as the network input features helps mitigate the influence of current variations under different operating conditions

$$\begin{cases} i^s_{x,n} = \dfrac{i^s_x}{\text{hypot}\left(i^s_\alpha, i^s_\beta\right)} \\ i^s_{y,n} = \dfrac{i^s_y}{\text{hypot}\left(i^s_\alpha, i^s_\beta\right)} \end{cases} \tag{14}$$

where $\text{hypot}(a,b) = \sqrt{a^2+b^2}$.

In the case of real-time input at the single sampling signals, the GRU layer in the neural network does not need to process historical data. The memoryless GRU degenerates into a combination of FC layers, as shown in (15), thereby reducing both data storage demand and computational load. In order to conveniently represent the degraded GRU layer, it is called GRU cell in this article. Compared to the MLP, this structure enhances the neural network's nonlinear computation capability

$$\begin{cases} \boldsymbol{f}_c = \boldsymbol{W}_c \boldsymbol{x} + \boldsymbol{b}_c \\ \boldsymbol{f}_u = \boldsymbol{W}_u \boldsymbol{x} + \boldsymbol{b}_u \\ \boldsymbol{H}_d = \tanh\left(\boldsymbol{f}_c\right) \cdot \left[1 - \text{sigmoid}\left(\boldsymbol{f}_u\right)\right] \end{cases} \tag{15}$$

where $\boldsymbol{x}$ and $\boldsymbol{H}_d$ represent the input and output vectors of the degenerate GRU, respectively. $\boldsymbol{W}_c$ and $\boldsymbol{W}_x$ are the weight matrices for the candidate gate and the update gate in the GRU network, while $\boldsymbol{b}_c$ and $\boldsymbol{b}_u$ are the corresponding bias terms.

In Fig. 12, BN represents the batch normalization (BN) layer. Adding this layer to the network effectively reduces the magnitude of gradient variations, preventing issues such as gradient explosion or vanishing gradients, and improves the convergence speed of training. Since the BN layer normalizes each batch during training, it introduces some degree of noise at a global level, affecting the direction of parameter convergence in a randomized manner. This effect helps reduce the model's dependence on specific data, enhancing its generalization ability.

The activation function $\tanh(x)$ is commonly used in neural networks, and its calculation formula is shown in (16). It involves two exponential operations of the natural constant e, which can be computationally expensive for embedded systems. Therefore, by converting (16) into Lambert's continued fractions (LCFs)[35], which involve seven divisions, and performing fraction reduction and simplification (detailed in Appendix B), the fitting formula shown in (17) can be derived

$$\tanh(x) = \frac{e^x - e^{-x}}{e^x + e^{-x}} \tag{16}$$

$$\mathscr{T}_7(x) = \frac{x\left(\left(\left(x^2+378\right)x^2+17325\right)x^2+135135\right)}{\left(\left(28x^2+3150\right)x^2+62370\right)x^2+135135}. \tag{17}$$

Fig. 13 illustrates the performance of the approximate function $\mathscr{T}_7(x)$ and $\mathscr{T}_5(x)$, here $\mathscr{T}_5(x)$ denotes the Lambert continued fraction expanded to five layers. It is worth noting that using LCF often encounters the issue of data divergence. For (17), when the input parameter range exceeds $[-4.97, 4.97]$, the output value will go beyond $[-1, 1]$. At $x = \pm 4.97$, the maximum approximate errors of $\mathscr{T}_7(x)$ and $\mathscr{T}_5(x)$ are $e^7_{\max} = \mp 9.58e-5$ and $e^5_{\max} = \pm 9.43e-4$, respectively, indicating the high approximation accuracy of $\mathscr{T}_7(x)$. The maximum errors $e^7_{\max}$ and $e^5_{\max}$ are directly added to the output of $\tanh(x)$ to evaluate the worst-case effect on the neural network softmax output, as shown in Fig. 14. The maximum error introduced by e^7_{max} is ∓ 0.0017, while that introduced by $e^5_{\max}$ is ± 0.0164. It is evident that the worst-case error of $\mathscr{T}_7(x)$ remains acceptable. For the

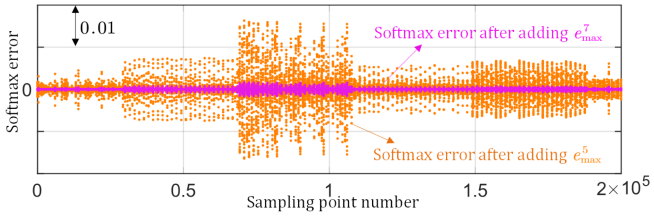

Fig. 14. Effect of worst-case approximation on neural network output.

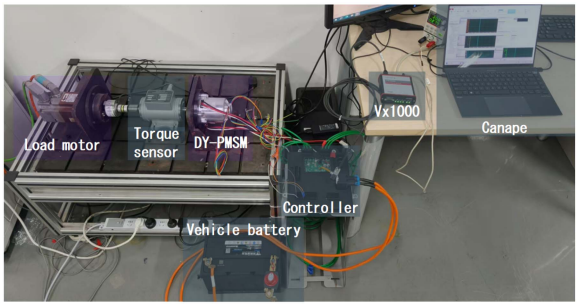

Fig. 15. DY-PMSM test bench.

Algorithm 1: Judgment of Output Fault State.

$\boldsymbol{S}_p$ denotes the set of 13 states of switches.

$if\ \ max(\boldsymbol{S}_p) > \tau$

$\quad output\ =\ Index(max(\boldsymbol{S}_p)) - 1$

end

where output = 0 means that the switches are in a healthy state, while outputs of 1, 2, ..., 12 correspond to open-circuit faults in T1, T2,..., T12, respectively. τ is a threshold value within the range [0,1].

application scenario presented in this article, the seven-layer Lambert continued fraction is sufficient. If higher accuracy or a wider input range is required, an LCF with more layers should be adopted.

Single-switch open-circuit faults require identifying the fault status of 12 switches as well as determining whether the system is operating normally. This represents a typical multiclass classification problem, for which softmax is the most suitable output function. Softmax outputs the probability of each switch being in an open-circuit fault, and the sum of these probabilities equals one. Therefore, additional judgment based on the pseudocode in algorithm 1 is required to finalize the fault state.

IV. Experimental Verification

The parameters of the DY-PMSM are shown in Table II. Fig. 15 shows the DY-PMSM and the experimental bench. The microcontroller unit is an Infineon TC399xp, while the driver chip is a TLE9183. In addition, a Vx1000, an online calibration and measurement device manufactured by Vector, is employed to collect real-time data transmitted by the algorithm at the sampling frequency. The developed algorithm is deployed on the AUTOSAR Classic Platform [36], and the controller is powered

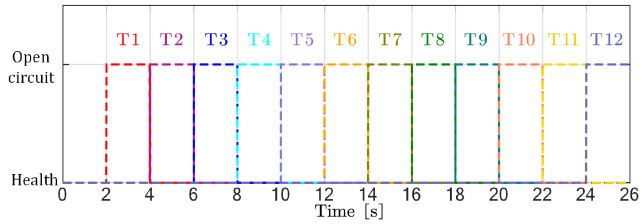

Fig. 16. Setting of the open-switch command.

TABLE III
Parameters of Training and Testing Datasets

Number	i_d^*	i_q^*	Speed	Purpose
Dataset 1	−1.0 A	10 A	100 rpm	Training
Dataset 2	−1.5 A	13 A	100 rpm	Training
Dataset 3	−2.0 A	16 A	100 rpm	Training
Dataset 4	−2.0 A	12 A	150 rpm	Testing
Dataset 5	−1.5 A	13 A	200 rpm	Testing

by a 12 V vehicle battery to closely replicate the real automotive operating conditions.

A. Acquisition of Experimental Datasets

The training and testing datasets were collected in the experiment using the open-circuit fault injection method described in (18). The open-switch commands are shown in Fig. 16, where each switch remained in an open-circuit fault state for 2 s before transitioning to the next switch fault. During this period, the speed of the load motor remained constant, and the current reference of the DY-PMSM was unchanged.

$$State:\ \text{health} \rightarrow \text{Ti-O} \rightarrow \text{health, i} = 1, 2, \ \ldots, \ 12 \qquad (18)$$

where Ti-O represents that the Ti switch is set to an open-circuit fault.

The experimental parameters are summarized in Table III. Retaining transitional state data in the dataset introduces considerable interference to the classifier, thereby increasing the difficulty for classification.

Note: When the switch is nonconducting, only the diode conducts the freewheeling current, resulting in minimal impact on the phase current regardless of whether an open-circuit fault occurs. To ensure consistency in evaluating the experimental results, this study assesses the health status of the switch only when it is conducting.

B. Comparative Analysis Based on Testing Datasets

The primary objective of the proposed algorithm is to achieve rapid open-circuit fault detection, enabling timely intervention of fault-tolerant control to reduce torque ripple. Therefore, the execution period of the fault diagnosis algorithm matches the sampling period $T_s = 50\ \mu$s. Fig. 17(a) and (b) compare the delay periods in identifying open-circuit fault states using the logic-based and data-driven methods under testing datasets 4 and 5, respectively. Here, N_d^{avg} and N_l^{avg} represent the average delay periods for fault detection using the data-driven and logic-based

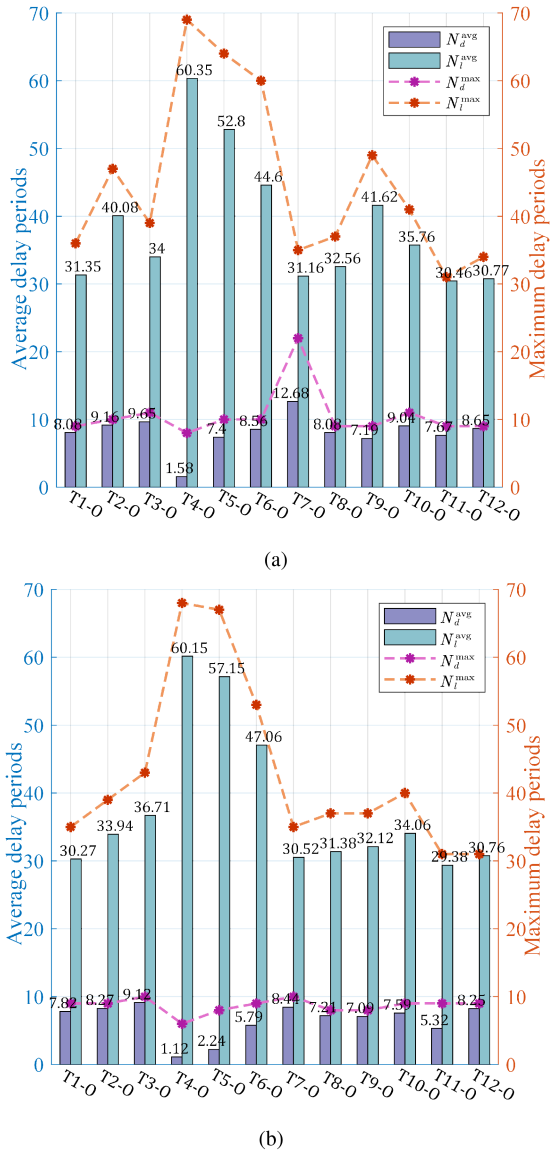

Fig. 17. Comparison of delay periods of data-driven and logic-based methods. (a) Based on dataset 4. (b) Based on dataset 5.

methods. $N_d^{\max}$ and $N_l^{\max}$ indicate the maximum delay periods observed in repeatedly open-switch fault tests for the data-driven and logic-based methods.

From the DY-PMSM's pole pair number is $n_p = 5$ and the sampling period is $T_s = 50\ \mu s$ given in Table II, one electrical cycle in datasets 4 and 5 corresponds to $N_{150} = 1600$ and $N_{200} = 1200$ can be calculated. As shown in Fig. 17, both proposed methods can identify the open-switch fault significantly shorter than one-quarter of an electrical cycle. Among them, the data-driven method demonstrates exceptionally high sensitivity, with an average fault detection delay of $N_d^{\text{avg}} = 7.33$ periods under the testing set, considerably lower than the logic-based method's average delay of $N_l^{\text{avg}} = 38.29$ periods. Moreover, the logic-based method exhibits fluctuations in fault detection time across different open-switch faults, with a maximum detection delay reaching $N_l^{\max} = 69$. In contrast, the data-driven method maintains a more stable detection time across various open-switch faults. The maximum delay curve only spikes to $N_d^{\max} = 22$ at one point in Fig. 17(a), while remaining consistently around 10in all other test scenarios.

TABLE IV
COMPARISON OF CLASSIFICATION ACCURACY

Figure number	A_d	A_a
Fig. 18 (a)	99.276%	99.995%
Fig. 18 (b)	98.921%	99.998%
Fig. 18 (c)	97.629%	99.999%
Fig. 18 (d)	98.015%	99.881%
Fig. 18 (e)	98.581%	99.993%
Fig. 18 (f)	97.349%	99.956%

To validate the effectiveness of the proposed method and further examine the impact of the filter window length n in (12) on the data-driven approach, Fig. 18(a)–(c) illustrate the confusion matrices obtained with different n. Moreover, when $n = 15$, the confusion matrices of the proposed network structure with recurrent state propagation, the CNN with one-dimensional convolution, and the logic-based method are also presented in Fig. 18(d)–(f), respectively. In this work, the accuracy considering all delayed state recognition data as misclassifications is defined as A_d, whereas the accuracy calculated by excluding delayed recognition errors is defined as A_a. The results summarized from the confusion matrices are provided in Table IV.

By combining the results in Table IV and Fig. 18, it can be observed that the parameter n correlates with both the misclassification rate and the classification delay in fault diagnosis. As n increases, the classification delay becomes longer, while the misclassification rate decreases. Therefore, the fault classification performance can be tuned by adjusting n. The GRU with recurrent state propagation exhibits short-term memory and simple gating rules. However, after incorporating recurrent states, the relatively low nonlinearity of its gating mechanism reduces the network sensitivity and classification accuracy, leading to the inferior performance observed in Fig. 18(d). The CNN with 1-D convolution achieves higher accuracy with a relatively small diagnostic delay. Although the optimized logic-based method in this work also provides high accuracy, it suffers from longer diagnostic delays. The results indicate that when $n = 15$, the proposed data-driven method [see Fig. 18(b)] achieves a balance between accuracy and diagnostic speed. Since the approaches used in Fig. 18(d) and (e) impose a relatively heavy computational burden, they are not deployable on embedded platforms for experimental validation. Therefore, the subsequent test-bench experiments primarily focus on demonstrating the performance of the proposed data-driven method and the logic-based method with $n = 15$.

C. DY-PMSM Open-Switch Fault Testing Under Steady Conditions

To evaluate the real-time performance and accuracy of the proposed open-circuit fault detection methods under different switch states and facilitate experimental analysis, three sets of open-switch tests were operated at 100 rpm. To ensure that

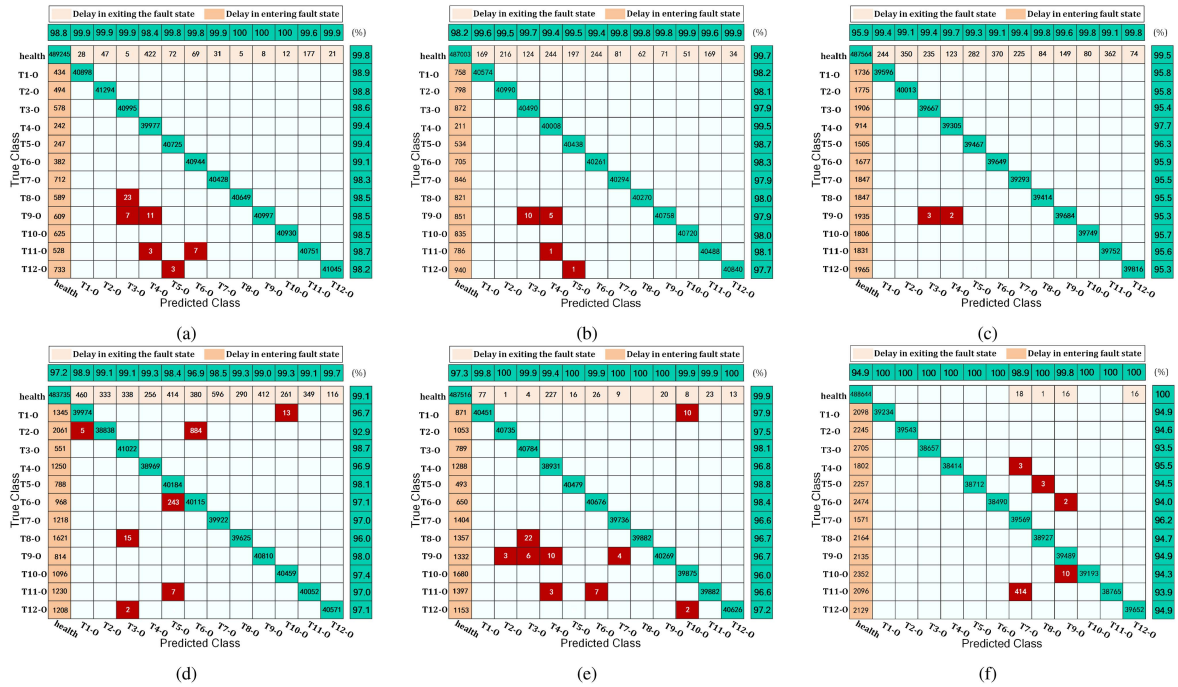

Fig. 18. Confusion matrix of datasets 4 and 5, where the red block means misclassification results. (a) Proposed data-driven method, $n = 5$. (b) Proposed data-driven method, $n = 15$. (c) Proposed data-driven method, $n = 25$. (d) Proposed network structure with recurrent state propagation, $n = 15$. (e) CNN with 1-D convolution, $n = 15$. (f) Logic-based method, $n = 15$.

the test current differs from the dataset, set $i^r_{d,\text{cmd}} = -0.134$ A and $i^r_{q,\text{cmd}} = 12.12$ A. Fig. 19 presents experiment I, where the T9 switch experiences an open-circuit fault before turning on. Fig. 20 shows experiment II, where the T5 switch encounters an open-circuit fault when the phase current is relatively low during conduction. Fig. 21 illustrates experiment III, where the T6 switch undergoes an open-circuit fault when the phase current is high during conduction. In addition, to evaluate the generalization ability and robustness of the proposed method under different rotational speeds, experiment IV, shown in Fig. 22, was operated at 400 rpm with the T7 switch experiencing an open-circuit fault, and set $i^r_{d,\text{cmd}} = -1.8$ A and $i^r_{q,\text{cmd}} = 17.0$ A.

In Fig. 19–22, F_d and F_l represent the switch numbers diagnosed by the data-driven and logic-based methods, respectively. As shown in (19), ΔN is the sampling period difference between the diagnosis output by data-driven and logic-based methods

$$\Delta N = N_l - N_d \tag{19}$$

where N_d and N_l represent the sampling period differences relative to the open-switch fault occurrence time for the diagnosis output by the data-driven and logic-based methods, respectively.

In Fig. 19, during the current flows into T3 and flows out from T7 and T8 in winding-I, an open-circuit fault is set on T9. Due to the open-circuit of T9, the parasitic diode voltage difference increases, causing a small attenuation in the positive current of phase-c. However, the impact on the phase current is relatively minor, and the phase open-circuit characteristic value and harmonic currents exhibit only small fluctuations. Thus, it is inappropriate to diagnose an open-circuit fault in this case. When the modulation strategy first switches to the scenario where the current flows out from T9, the open-circuit fault at T9 causes the phase open-circuit characteristic value to increase rapidly. At this point, the values of $i^s_{x,n}$ and $i^s_{y,n}$ are smaller, and F_d can quickly locate the open-circuit switch. However, F_l experiences a delay of 45 sampling periods relative to F_d. From the T9 open-circuit test shown in Fig. 19, it can be observed that both F_d and F_l can accurately locate the faulty switch, with F_d exhibiting faster fault localization performance. This demonstrates the effectiveness of the proposed method in terms of both accuracy and speed in detecting an open-switch fault.

In Fig. 20, the T5 switch is set to an open-circuit fault when T5 conducts with a relatively small phase current. At this moment, the values of $i^s_{x,n}$ and $i^s_{y,n}$ caused by the open-circuit fault are small, making it difficult to locate the faulty switch. From the fault localization comparison results, it can be seen that F_l is delayed by 32 sampling cycles relative to F_d. Moreover, during the detection process, F_l produces an incorrect output, misidentifying the open-circuit fault of T5 as T8. The data-driven method does not produce misjudgments even when the fault characteristic input values are small, while maintaining rapid detection. As the motor position and the modulation strategy change, causing T5 to conduct again, F_d detects the open-circuit fault of T5 77 sampling cycles earlier than F_l. The primary reason the data-driven method is more accurate and faster than the logic-based method is that the former learns from a large amount of experimental data to abstract the relationship between open-circuit characteristic values and the faulty switch location. In contrast, the latter relies on logical rules and threshold values for judgment, making it difficult to adapt to open-circuit faults under low current conditions.

In Fig. 21, the T6 switch open-circuit fault occurs when T6 is conducting, and the phase current is near its peak. Since the

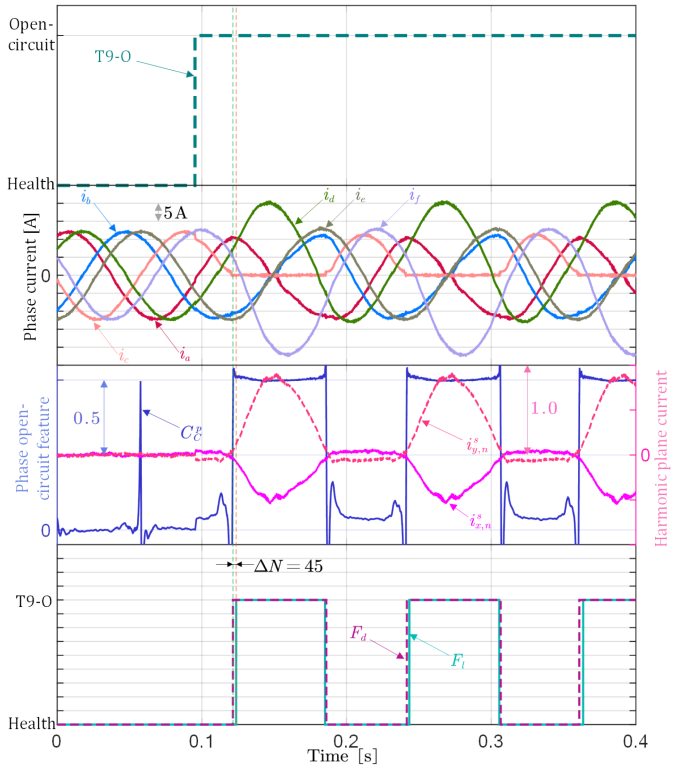

Fig. 19. Experiment I: The T9 switch has an open-circuit fault.

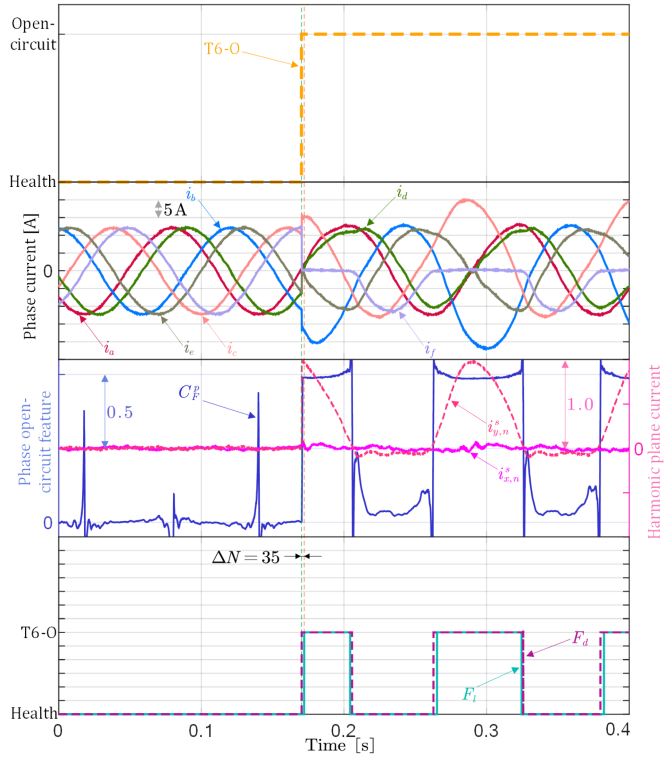

Fig. 21. Experiment III: The T6 switch has an open-circuit fault.

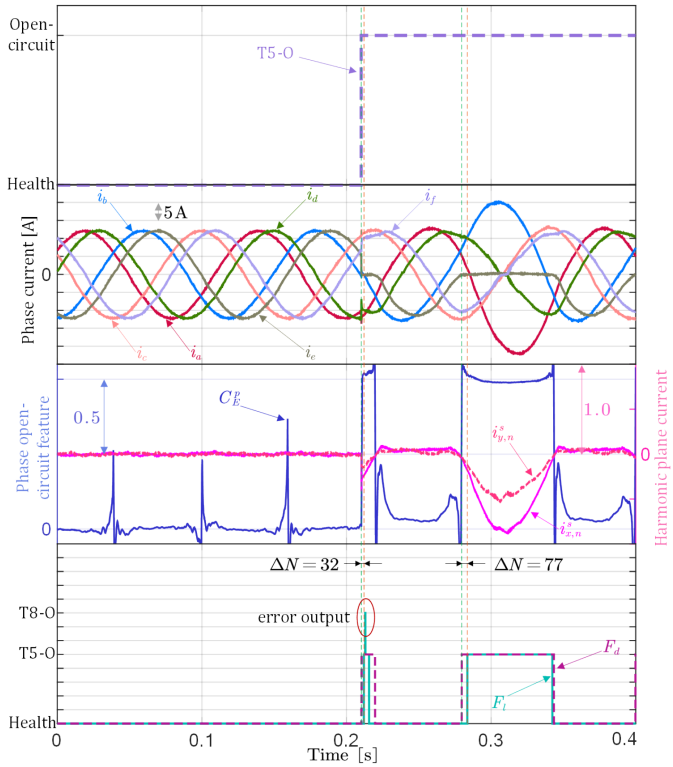

Fig. 20. Experiment II: The T5 switch has an open-circuit fault.

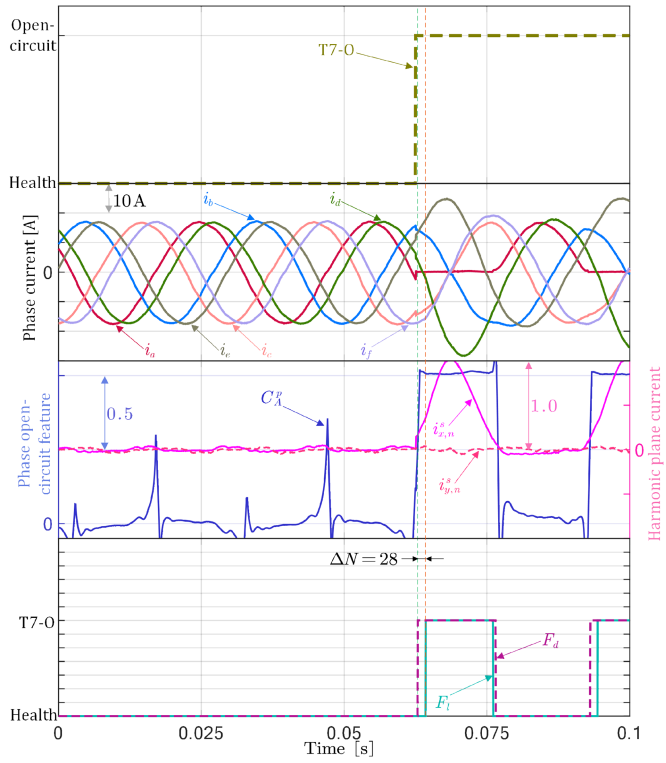

Fig. 22. Experiment IV: The T7 switch has an open-circuit fault.

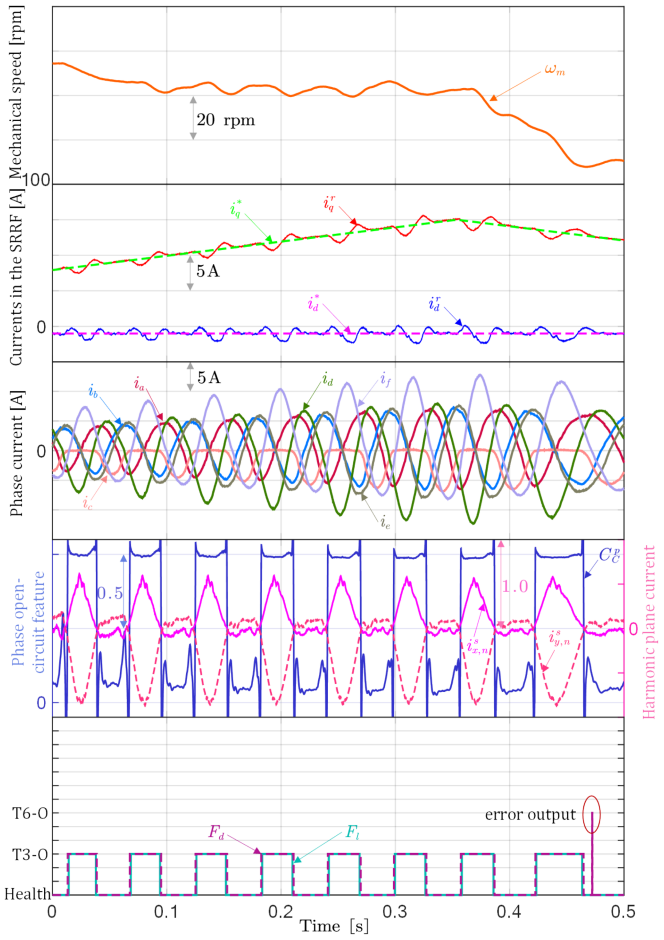

Fig. 23. T3 switch was kept open-circuited during the experiment, with a q-axis current command variation rate of 20A/s.

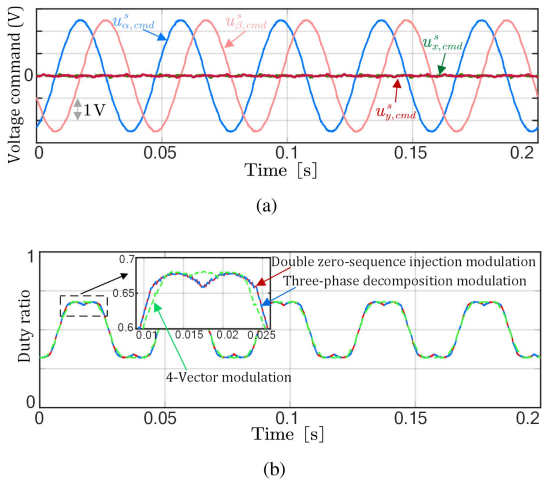

Fig. 24. Modulation algorithm comparison. (a) Voltage commands. (b) Duty ratios of phase-a.

harmonic subspace currents are normalized to $i^s_{x,n}$ and $i^s_{y,n}$, their maximum value is close to 1.0, which facilitates fault location by the algorithm. From the fault diagnosis results in Fig. 21, it can be observed that both F_l and F_d accurately locate the open-circuit fault at T6.

In experiment IV shown in Fig. 22, when T7 experiences an open-circuit fault, the phase current is extremely small, approximately –2.4 A. The data-driven method correctly outputs the open-circuit diagnosis result within eight sampling periods after the fault command. In contrast, the logic-based method fails to identify the open-circuit fault under low phase current conditions accurately. It only outputs the correct diagnosis after the harmonic subspace current increases, resulting in a delay of 36 sampling periods in open-switch localization. From Fig. 22, it can be seen that in the open-circuit fault test at 400 rpm, a speed condition much higher than that of the training set does not interfere with the data-driven method. This is because the proposed open-circuit fault diagnosis algorithm does not use speed and position signals as input features.

In Fig. 19 through Fig. 22, compared with the logic-based method, the data-driven method consistently exhibits earlier fault activation and delayed fault exit. This behavior is consistent with the confusion matrix analysis of the test datasets presented in Fig. 18.

In Experiments II, III, and IV, the data-driven method first located the fault in five, two, and eight sampling periods, accounting for 0.21%, 0.083%, and 1.33% of the electrical period, respectively. The logic-based method required 37, 37, and 36 sampling periods, corresponding to 1.54%, 1.54%, and 6.0% of the electrical period. This demonstrates that both proposed methods have highly rapid fault detection and localization capabilities.

The proposed data-driven method was trained on a dataset containing switch open-circuit faults under only three current operating conditions, with a total of 1.578 million sampling points. Unlike other data-driven fault diagnosis algorithms, which generally include only current data under typical open-circuit conditions, this study retains all transition data before and after the open-circuit event, and the effects of these transitions on current fluctuations were not excluded. Experimental results demonstrate that the data-driven method exhibits strong generalization ability and real-time performance.

D. DY-PMSM Open-Switch Fault Testing Under Dynamic Condition

In the dynamic operating condition, the T3 switch is set to the open-circuit state, and the variation rate of the q-axis current command i^*_q in the SRRF is set to 20A/s. The SRRF current commands i^*_d and i^*_q, together with the actual currents i^r_d and i^r_q, are shown in the second subfigure of Fig. 23. The speed variation during the experiment is shown in the first subfigure of Fig. 23. It can be observed that under dynamic conditions, the effective range of the phase open-circuit feature value remains within [0,1], the speed variation only affects the duration of the feature value without influencing its magnitude. Moreover, $i^s_{x,n}$ and $i^s_{y,n}$ exhibit no distortion.

From the fault diagnosis results, it is evident that the proposed data-driven method still demonstrates high sensitivity and can accurately identify the faulty switch earlier than the logic-based

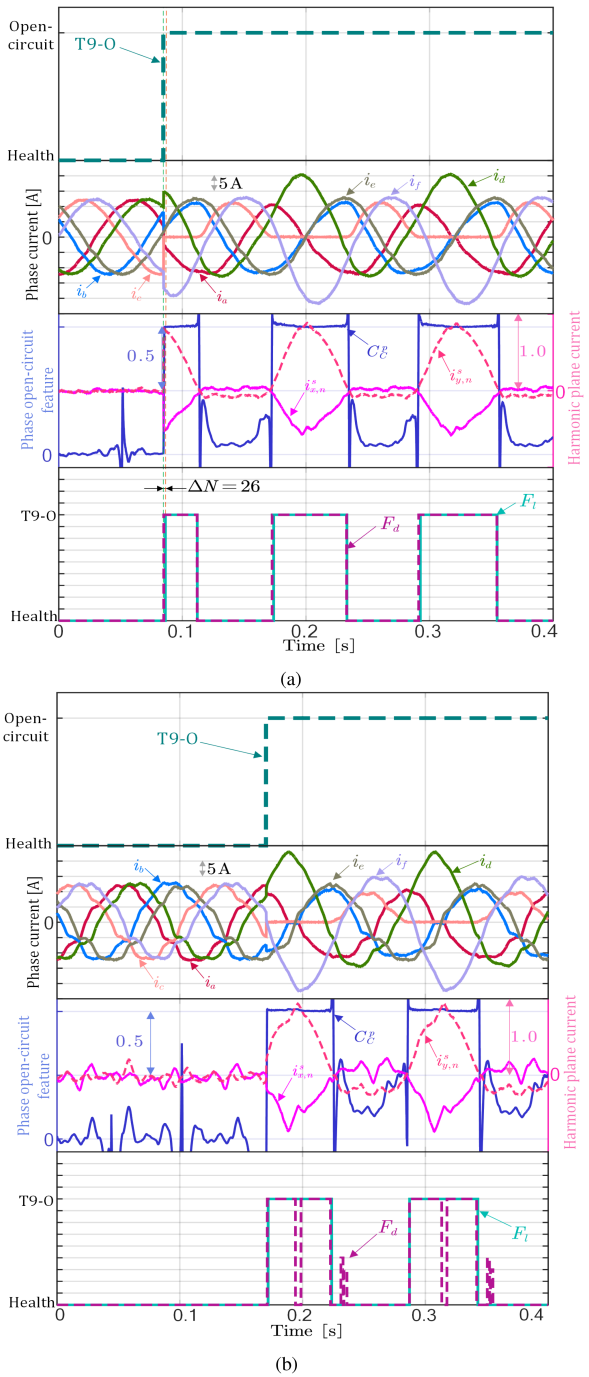

Fig. 25. T9 switch has an open-circuit fault under different modulation algorithms. (a) Three-phase decomposition modulation. (b) Four-vector modulation.

method. However, a false judgment occurs at 0.4721 s, lasting for two periods, which indicates that the generalization ability of the classification network still requires improvement. This can be achieved by moderately increasing the network complexity in accordance with the performance of the embedded system or by enlarging the training dataset.

E. Performance Under Different Modulation Algorithms

In the above-mentioned work, all processes including data acquisition, network training, and experimental testing of the proposed method were carried out under double zero-sequence injection modulation [37]. To evaluate the performance of the proposed method under different PWM modulation strategies, the network parameters trained under double zero-sequence injection modulation were directly applied for testing under the three-phase decomposition modulation [38] and four-vector modulation [39] methods.

In the simulation environment, the duty ratios of phase-a calculated under double zero-sequence injection modulation, three-phase decomposition modulation, and four-vector modulation for the voltage command shown in Fig. 24(a) are presented in Fig. 24(b). Where $u^s_{\alpha,\mathrm{cmd}}$ and $u^s_{\beta,\mathrm{cmd}}$ represent the voltage commands in the electromechanical energy conversion subspace, while $u^s_{x,\mathrm{cmd}}$ and $u^s_{y,\mathrm{cmd}}$ correspond to the voltage commands in the harmonic subspace. As shown in Fig. 24(b), the duty ratios obtained from double zero-sequence injection modulation and three-phase decomposition modulation are nearly identical, while the four-vector modulation exhibits a distinctly different duty ratio waveform due to the open-loop control applied in the harmonic subspace.

In Fig. 25, the performance of the proposed algorithm under the three-phase decomposition modulation and four-vector modulation schemes is evaluated, using the same test conditions as in Fig. 19. From Fig. 25(a), it can be observed that the data-driven method achieves accurate fault localization significantly earlier than the logic-based method. In contrast, as shown in Fig. 25(b), the four-vector modulation employs an open-loop harmonic suppression strategy that restricts the modulation voltage in the harmonic subspace. This results in severe distortion of the phase currents, and the harmonic features $i^s_{x,n}$ and $i^s_{y,n}$ exhibit much stronger fluctuations compared to other modulation strategies, as seen in Figs. 19 and 25(a). Consequently, the data-driven method is subjected to substantial interference. Nevertheless, since the data-driven method determines fault states based on the polar coordinate trajectory of harmonic subspace currents, it demonstrates stronger robustness against such disturbances.

It should be emphasized that the data-driven method tested in Fig. 25 was trained under the double zero-sequence injection modulation scheme. Therefore, this serves as a challenging test case for the neural network. Despite this, the proposed method successfully identifies the faulty switch in most data samples.

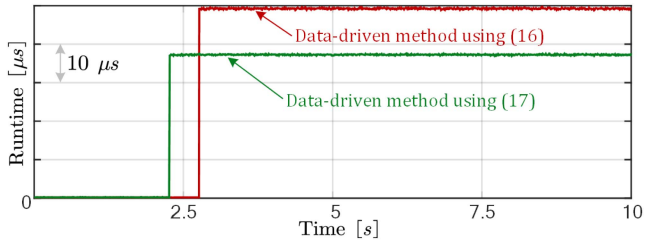

Fig. 26. Comparison of neural network computation time using different activation function computation methods.

F. Runtime Comparison

To meet the real-time requirements of neural network operation on the embedded platform, all parameter data types of the

deep learning network shown in Fig. 12 are set to float32 during deployment. Fig. 26 presents a comparison of the running time of the data-driven method using (16) and (17) for the calculation of the activation function $\tanh(x)$. The average time consumption for (16) is 49.24 μ s, while that for (17) is 37.26 μs. Since $\tanh(x)$ is used multiple times in the designed neural network, the fitting method based on (17) reduces computation time by 24.3% compared to directly calculating $\tanh(x)$ using (16).

V. Conclusion

This article focuses on the rapid and accurate open-switch fault diagnosis and localization of the DY-PMSM under the limited computational resources of embedded platforms.

This article proposes two open-circuit fault diagnosis methods for power switches. Essentially, both approaches rely on the same feature values and motor state variables for judgment. The logic-based method uses a cascaded triggering logic, while the neural network directly extracts open-switch features from input samples to perform fault diagnosis and localization. To reduce the difficulty of labeling and classifying large amounts of experimental data and to avoid coupling between the data-driven method and logic-based method, this article designs an autoencoder-assisted dataset generation approach. In addition, a high-precision fitting algorithm for neural network activation functions is proposed to enhance the computational efficiency of the network.

The effectiveness of the proposed methods is validated through open-circuit fault experiments. The experimental results demonstrate that the proposed data-driven method achieves high diagnostic accuracy and low latency under various operating conditions. Moreover, the computation is completed within 50 μs, confirming the methods' suitability for embedded platform applications.

The remaining issues of the proposed method are summarized as follows.

1) *Multiple open-circuit faults:* When several switches are open-circuited, the harmonic subspace trajectory exhibits a sector shape, as shown in Fig. 4. However, the sector arc may overlap with the current trajectory angle of healthy switches. In this case, evaluating the variation rate of the current trajectory radius could provide an auxiliary means for fault localization.
2) *Applicability to different multiphase machines:* The motor state variables employed in the proposed method are all derived from the VSD transformation theory, which theoretically ensures applicability to any multiphase machine topology. Nevertheless, further experimental validation has not yet been conducted due to equipment constraints.

Appendix A
Activations and Learnable Sizes of Proposed Deep Learning Networks

A Offline Fault Data Labeling Network

The activations and learnable sizes of the neural network in Fig. 8 are listed in Table V. The layers in the table are arranged in the same top-to-bottom order as shown in Fig. 8. Here, weights (I) denotes the input weights, and weights (R) denotes the recurrent weights. C, B, and T represent channel, batch, and time steps, respectively.

TABLE V
Activations and Learnable Sizes of the Data Labeling Network

Type	Activations	Learnable sizes
Sequence input	$6(C)\times1(B)\times12(T)$	–
LSTM	$12(C)\times1(B)\times12(T)$	Weights (I) 48×6; Weights (R) 48×12; Bias 48×1
GRU	$12(C)\times1(B)\times12(T)$	Weights (I) 36×6; Weights (R) 36×12; Bias 36×1
Addition	$12(C)\times1(B)\times12(T)$	–
1-D convolution	$6(C)\times1(B)\times12(T)$	Weights $6\times12\times6$; Bias 1×6
1-D average pooling	$6(C)\times1(B)\times12(T)$	–
1-D convolution	$6(C)\times1(B)\times12(T)$	Weights $3\times6\times6$; Bias 1×6
1-D average pooling	$6(C)\times1(B)\times12(T)$	–
Fully connected	$32(C)\times1(B)\times12(T)$	Weights 32×6; Bias 32×1
ReLU	$32(C)\times1(B)\times12(T)$	–
BN	$32(C)\times1(B)\times12(T)$	Offset 32×1; Scale 32×1
Fully connected	$6(C)\times1(B)\times12(T)$	Weights 6×32; Bias 6×1

The data dimensions in Table V are not fixed, since this network is used for offline data processing and does not have strict computation time requirements. The data dimensions can be adjusted within an acceptable reconstruction error range of $|C_*^p - \hat{C}_*^p| < 0.1$.

B Online Fault Diagnosis Network

The activations and learnable sizes of the neural network in Fig. 12 are listed in Table VI. The layers in the table are arranged from left to right, consistent with Fig. 12. Since this network uses feature-based inputs, there is no time steps dimension, and all weights (R) are zero matrices.

The design criterion for the data dimensions of the fault diagnosis network in Fig. 12 is to maximize fault detection accuracy within a limited computation time. The data dimensions in Table VI were determined through repeated testing. As shown in Fig. 26, the unoptimized original network already reaches the 50 μs runtime boundary.

Appendix B
Lambert Continued Fraction

The Lambert continued fraction constructs a multilayered fraction through rational approximation, which is then truncated and reduced to polynomial forms of the numerator and denominator. Its general form is given in (B.1)

$$\begin{cases} \tanh(x) = \frac{x}{\mathscr{L}_k} \\ \mathscr{L}_k = (2k-1) + \frac{x^2}{\mathscr{L}_{k+1}} \end{cases} \tag{B.1}$$

TABLE VI
ACTIVATIONS AND LEARNABLE SIZES OF THE ONLINE FAULT DIAGNOSIS NETWORK

Type	Activations	Learnable Sizes
Feature input	$8(C) \times 1(B)$	–
GRU cell	$6(C) \times 1(B)$	Weights (I) 18×8; Weights (R) zeros(18,6); Bias 18×1
GRU cell	$6(C) \times 1(B)$	Weights (I) 18×6; Weights (R) zeros(18,6); Bias 18×1
Fully connected	$6(C) \times 1(B)$	Weights 6×8; Bias 6×1
Fully connected	$6(C) \times 1(B)$	Weights 6×6; Bias 6×1
Addition	$6(C) \times 1(B)$	–
GRU cell	$6(C) \times 1(B)$	Weights (I) 18×6; Weights (R) zeros(18,6); Bias 18×1
BN	$6(C) \times 1(B)$	Offset 6×1; Scale 6×1
Fully connected	$6(C) \times 1(B)$	Weights 6×6; Bias 6×1
Fully connected	$6(C) \times 1(B)$	Weights 6×6; Bias 6×1
Fully connected	$9(C) \times 1(B)$	Weights 9×6; Bias 9×1
Fully connected	$9(C) \times 1(B)$	Weights 9×9; Bias 9×1
Tanh	$9(C) \times 1(B)$	–
Fully connected	$13(C) \times 1(B)$	Weights 13×9; Bias 13×1
Fully connected	$13(C) \times 1(B)$	Weights 13×13; Bias 13×1
Fully connected	$13(C) \times 1(B)$	Weights 13×13; Bias 13×1
Softmax	$13(C) \times 1(B)$	–

where k is a nonzero positive integer. According to the number of expansion layers, the approximated function is denoted as $\mathscr{T}_k(x)$.

When the continued fraction is expanded to $k = 7$, the expression of $\mathscr{T}_7(x)$ is shown in (B.2)

$$\tanh(x) \approx \mathscr{T}_7(x) = \cfrac{x}{1 + \cfrac{x^2}{3 + \cfrac{x^2}{5 + \cfrac{x^2}{7 + \cfrac{x^2}{9 + \cfrac{x^2}{11 + \cfrac{x^2}{13}}}}}}}. \quad \text{(B.2)}$$

Expanding (B.2) bottom-up and reducing it to a common denominator yields a polynomial ratio with an odd-order numerator and an even-order denominator. After normalizing the constant factors to integer coefficients, (B.3) is obtained

$$\mathscr{T}_7(x) = \frac{x\left(x^6 + 378x^4 + 17325x^2 + 135135\right)}{28x^6 + 3150x^4 + 62370x^2 + 135135}. \quad \text{(B.3)}$$

To further avoid exponential operations of high-order terms, (B.3) is reformulated into the nested multiplicative form shown in (17).

REFERENCES

[1] L. Vancini, M. Mengoni, G. Rizzoli, A. Bellini, L. Zarri, and A. Tani, "Online temperature estimation of stator windings and rotor magnets for six-phase permanent magnet synchronous motors," in *Proc. Int. Conf. Elect. Mach.*, 2022, pp. 1555–1561.

[2] R. Zhang, X. Li, J. Ding, S. Chen, H. Yang, and H. Guo, "Review of IGBT intelligent gate drive and protection strategies," *IEEE Trans. Power Electron.*, vol. 39, no. 6, pp. 7392–7403, Jun. 2024.

[3] J. Sun, C. Li, Z. Zheng, K. Wang, and Y. Li, "A generalized, fast and robust open-circuit fault diagnosis technique for star-connected symmetrical multiphase drives," *IEEE Trans. Energy Conver.*, vol. 37, no. 3, pp. 1921–1933, Sep. 2022.

[4] Z. Song, F. Zhou, Y. Yu, R. Zhang, and S. Hu, "Open-phase fault-tolerant predictive control strategy for open-end-winding permanent magnet synchronous machines without postfault controller reconfiguration," *IEEE Trans. Ind. Electron.*, vol. 68, no. 5, pp. 3770–3781, May 2021.

[5] Q. Liu, L. Xiao, Q. Wu, X. Zhao, and Y. Liu, "An adaptive fault-tolerant control without fault location of open-phase fault for dual three-phase PMSM drive system," *IEEE J. Emerg. Sel. Topics Power Electron.*, vol. 13, no. 3, pp. 3516–3528, Jun. 2025.

[6] C. J. Gajanayake, B. Bhangu, S. Nadarajan, and G. Jayasinghe, "Fault tolerant control method to improve the torque and speed response in PMSM drive with winding faults," in *Proc. IEEE 9th Int. Conf. Power Electron. Drive Syst.*, 2011, pp. 956–961.

[7] M. Salman, J. Riccio, S. K. E. Khil, P. Zanchetta, and C. Boccaletti, "Unified diagnosis and localization method of open switch faults in voltage source inverters-fed synchronous reluctance motors," *IEEE Trans. Ind. Appl.*, vol. 61, no. 6, pp. 9517–9528, Nov./Dec. 2025.

[8] Y. Zhang, Y. Mao, X. Wang, Z. Wang, D. Xiao, and G. Fang, "Current prediction-based fast diagnosis of electrical faults in PMSM drives," *IEEE Trans. Transp. Electrif.*, vol. 8, no. 4, pp. 4622–4632, Dec. 2022.

[9] W. Huang et al., "Current-based open-circuit fault diagnosis for PMSM drives with model predictive control," *IEEE Trans. Power Electron.*, vol. 36, no. 9, pp. 10695–10704, Sep. 2021.

[10] J. Hang, H. Wu, J. Zhang, S. Ding, Y. Huang, and W. Hua, "Cost function-based open-phase fault diagnosis for PMSM drive system with model predictive current control," *IEEE Trans. Power Electron.*, vol. 36, no. 3, pp. 2574–2583, Mar. 2021.

[11] X. Chen, J. Liu, Z. Deng, S. Song, S. Du, and D. Wang, "A diagnosis strategy for multiple IGBT open-circuit faults of modular multilevel converters," *IEEE Trans. Power Electron.*, vol. 36, no. 1, pp. 191–203, Jan. 2021.

[12] M. A. Rodríguez-Blanco et al., "A failure-detection strategy for IGBT based on gate-voltage behavior applied to a motor drive system," *IEEE Trans. Ind. Electron.*, vol. 58, no. 5, pp. 1625–1633, May 2011.

[13] P. F. Goncalves, S. M. Cruz, and A. M. Mendes, "Online diagnostic method for the detection of high-resistance connections and open-phase faults in six-phase PMSM drives," *IEEE Trans. Ind. Applicat.*, vol. 58, no. 1, pp. 345–355, Jan./Feb. 2022.

[14] X. Wang, Z. Wang, Z. Xu, M. Cheng, W. Wang, and Y. Hu, "Comprehensive diagnosis and tolerance strategies for electrical faults and sensor faults in dual three-phase PMSM drives," *IEEE Trans. Power Electron.*, vol. 34, no. 7, pp. 6669–6684, Jul. 2019.

[15] M. Trabelsi, N. K. Nguyen, and E. Semail, "Real-time switches fault diagnosis based on typical operating characteristics of five-phase permanent-magnetic synchronous machines," *IEEE Trans. Ind. Electron.*, vol. 63, no. 8, pp. 4683–4694, Aug. 2016.

[16] M. J. Duran, I. Gonzalez-Prieto, N. Rios-Garcia, and F. Barrero, "A simple, fast, and robust open-phase fault detection technique for six-phase induction motor drives," *IEEE Trans. Power Electron.*, vol. 33, no. 1, pp. 547–557, Jan. 2018.

[17] Y. Wu and L. Peretti, "Detection of multiple open faults in variable phase-pole machines based on harmonic plane decomposition," in *Proc. IEEE 14th Int. Symp. Diagnostics Elect. Mach.*, 2023, pp. 141–146.

[18] Y. Wu, G. F. Olson, C. Henriksson, and L. Peretti, "Open fault detection in variable phase-pole machines based on harmonic plane decomposition," *IEEE Trans. Power Electron.*, vol. 39, no. 4, pp. 4557–4566, Apr. 2024.

[19] T. Li, R. Ma, and Z. Zhang, "Diagnosis of open-phase fault of five-phase permanent magnet synchronous motor by harmonic current analysis," *Microelectron. Reliab.*, vol. 126, pp. 1–5, Nov. 2021.

[20] H. Chen, J. He, N. A. Demerdash, X. Guan, and C. H. Lee, "Diagnosis of open-phase faults for a five-phase PMSM fed by a closed-loop vector-controlled drive based on magnetic field pendulous oscillation technique," *IEEE Trans. Ind. Electron.*, vol. 68, no. 7, pp. 5582–5593, Jul. 2021.

[21] A. S. Gardouh, S. Abulanwar, F. Deng, E. Gouda, and A. Ghanem, "Novel unified normalized DC current-based diagnosis scheme of interturn and open-switch faults for VSI-fed induction motor drive system," *IEEE Trans. Power Electron.*, vol. 40, no. 10, pp. 14710–14721, Oct. 2025.
[22] A. G. Yepes, I. Gonzalez-Prieto, O. Lopez, M. J. Duran, and J. Doval-Gandoy, "A comprehensive survey on fault tolerance in multiphase ac drives, Part 2: Phase and switch open-circuit faults," *Machines*, vol. 10, no. 3, Mar. 2022, Art. no. 2.
[23] Y. Xia, Y. Xu, and B. Gou, "A data-driven method for IGBT open-circuit fault diagnosis based on hybrid ensemble learning and sliding-window classification," *IEEE Trans Ind. Informat.*, vol. 16, no. 8, pp. 5223–5233, Aug. 2020.
[24] B. Gou, Y. Xu, Y. Xia, Q. Deng, and X. Ge, "An online data-driven method for simultaneous diagnosis of IGBT and current sensor fault of three-phase PWM inverter in induction motor drives," *IEEE Trans. Power Electron.*, vol. 35, no. 12, pp. 13281–13294, Dec. 2020.
[25] J. Hang, X. Shu, S. Ding, and Y. Huang, "Robust open-circuit fault diagnosis for PMSM drives using wavelet convolutional neural network with small samples of normalized current vector trajectory graph," *IEEE Trans. Ind. Electron.*, vol. 70, no. 8, pp. 7653–7663, Aug. 2023.
[26] L. Guo, Y. Lei, S. Xing, T. Yan, and N. Li, "Deep convolutional transfer learning network: A new method for intelligent fault diagnosis of machines with unlabeled data," *IEEE Trans. Ind. Electron.*, vol. 66, no. 9, pp. 7316–7325, Sep. 2019.
[27] J. Hang, G. Qiu, M. Hao, and S. Ding, "Improved fault diagnosis method for permanent magnet synchronous machine system based on lightweight multisource information data layer fusion," *IEEE Trans. Power Electron.*, vol. 39, no. 10, pp. 13808–13817, Oct. 2024.
[28] S. Rokocakau et al., "Fault diagnosis using shallow neural networks for voltage source inverters in motor drives," *IEEE Trans. Ind. Applicat.*, vol. 60, no. 5, pp. 7038–7047, Sep.–Oct. 2024.
[29] L. Jin, Y. Mao, X. Wang, L. Lu, and Z. Wang, "Online data-driven fault diagnosis of dual three-phase PMSM drives considering limited labeled samples," *IEEE Trans. Ind. Electron.*, vol. 71, no. 7, pp. 6797–6808, Jul. 2024.
[30] L. Jin, X. Wang, Y. Mao, L. Lu, and Z. Wang, "Online attribute matching based few-sample data-driven diagnosis of electrical faults in PMSM drive," *IEEE Trans. Power Electron.*, vol. 39, no. 2, pp. 2620–2631, Feb. 2024.
[31] Z. Liu, L. Fang, D. Jiang, and R. Qu, "A machine-learning-based fault diagnosis method with adaptive secondary sampling for multiphase drive systems," *IEEE Trans. Power Electron.*, vol. 37, no. 8, pp. 8767–8772, Aug. 2022.
[32] Y. Hu, Z. Q. Zhu, and K. Liu, "Current control for dual three-phase permanent magnet synchronous motors accounting for current unbalance and harmonics," *IEEE J. Emerg. Sel. Topics Power Electron.*, vol. 2, no. 2, pp. 272–284, Jun. 2014.
[33] H. Zhu and H. Fujimoto, "Suppression of current quantization effects for precise current control of SPMSM using dithering techniques and Kalman filter," *IEEE Trans Ind. Informat.*, vol. 10, no. 2, pp. 1361–1371, May 2014.
[34] Z. F. Zhang, Y. Wu, and S. Y. Qi, "Diagnosis method for open-circuit faults of six-phase permanent magnet synchronous motor drive system," *IET Power Electron.*, vol. 13, no. 15, pp. 3305–3313, Nov. 2020.
[35] C. B. Corcino, R. B. Corcino, and I. Mező, "Continued fraction expansions for the lambert w function," *Aequationes Mathematicae*, vol. 93, no. 2, pp. 485–498, 2019.
[36] M. Staron, *AUTOSAR (AUTomotive Open System ARchitecture)*. Berlin, Germany: Springer, 2021, pp. 97–136.
[37] R. Bojoi, M. Lazzari, F. Profumo, and A. Tenconi, "Digital field-oriented control for dual three-phase induction motor drives," *IEEE Trans. Ind. Applicat.*, vol. 39, no. 3, pp. 752–760, May/Jun. 2003.
[38] G. Grandi, G. Serra, and A. Tani, "Space vector modulation of a six-phase VSI based on three-phase decomposition," in *Proc. Int. Symp. Power Electronics, Elect. Drives, Automat. Motion*. Ischia, Italy, Jun. 2008, pp. 674–679.
[39] D. Hadiouche, L. Baghli, and A. Rezzoug, "Space-vector PWM techniques for dual three-phase AC machine: Analysis, performance evaluation, and DSP implementation," *IEEE Trans. Ind. Applicat.*, vol. 42, no. 4, pp. 1112–1122, Jul./Aug 2006.

Shihan Xu was born in Anhui, China, in 1997. He received the B.S. degree from Shenyang Ligong University, Shenyang, China, in 2019, and the M.Eng. degree from the School of Automotive and Transportation Engineering, Hefei University of Technology, Hefei, China, in 2022, both in vehicle engineering. He is currently working toward the Ph.D. degree in vehicle engineering with the School of Automotive Studies, Tongji University, Shanghai, China,

He is a Visiting Ph.D. Student with the Department of Electrical, Electronic, and Information Engineering "Guglielmo Marconi," University of Bologna, Bologna, Italy. His research interests include parameter identification of PMSMs, fault diagnosis methods for multiphase PMSMs, and vehicle dynamics.

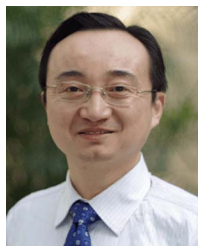

Yuan Zhu was born in Jiangsu, China, in 1976. He received the double B.S. degrees in automotive engineering and computer application technology, and the Ph.D. degree in automotive engineering from Tsinghua University, Beijing, China, in 1998 and 2003, respectively.

From 2003 to 2005, he was an Assistant Research Scientist with the Department of Automotive Engineering, Tsinghua University. Since 2005, he has been an Associate Professor with the Sino-German School and the School of Automotive Studies, Tongji University, Shanghai, China. From 2014 to 2019, he held the Hans L. Merkle Foundation-Bosch Endowed Chair for Automotive Systems with Tongji University. Since 2023, he has been the Director with the School of Automotive Studies, Tongji University-Vector Automotive Technology Joint Laboratory. Since 2024, he has held the Infineon Endowed Chair for Microcontroller and Embedded Systems with Tongji University. His research interests include control and parameter identification for electric drive systems and high-speed PMSMs, as well as embedded software systems.

Luca Zarri (Senior Member, IEEE) received the M.Sc. and Ph.D. degrees in electrical engineering from the University of Bologna, Bologna, Italy, in 1998 and 2007, respectively.

He is currently a Full Professor of power electronics, electrical machines and drives with the Department of Electrical, Electronic, and Information Engineering "Guglielmo Marconi", University of Bologna. He has authored or coauthored more than 200 scientific papers. His research interests include the control of power converters and electric drives.

Dr. Zarri is a Senior Member of the IEEE Industry Applications, IEEE Power Electronics, and IEEE Industrial Electronics Societies. Currently, he is the Vice Chair of the IEEE IAS Industrial Power Conversion Systems Department.